

Manipulating the K-Space
for Reduction of Respiratory Induced Motion Artifacts

by

MAIDA RANJBAR

Presented to the Faculty of the Graduate School of
The University of Texas at Arlington in Partial Fulfillment
of the Requirements
for the Degree of

MASTER OF SCIENCE

THE UNIVERSITY OF TEXAS AT ARLINGTON

May 2016

ACKNOWLEDGEMENTS

I would like to thank my supervisor Dr. Ananth Madhuranthakam for his patience and support. This dissertation would not have been possible without his guidance and help.

I would also like to express my gratitude to my defence committee members professors Hanli Liu, and Michael Cho for their valuable feedback, guidance and time. Additionally, I am thankful to Dr. Rajiv Chopra for having provided me with the opportunity to serve in his research group.

Finally, I would like to thank my dearest family and Pouya for their tremendous support over the course of my studies. Their positive reinforcement and encouragement has been my motivation for pushing forward and succeeding.

May, 2016

ABSTRACT

Manipulating the K-Space for Reduction of Respiratory Induced Motion Artifacts

Maida Ranjbar, M.Sc.

The University of Texas at Arlington, 2016

Supervising Professor: Dr. Ananth Madhuranthakam

Respiratory induced motion artifacts, particularly those occurring in the abdomen and lung, pose a hefty problem in current diagnostic MR imaging. Application of images plagued with such artifacts not only hinder diagnosis, but may result in the enforcement of undesirably large safety margins in radiation therapy due to un-captured tumor characteristics that are concealed by the artifact. While several methods such as gated scans, breath-hold scans, variation of the K-Space acquisition trajectory, and reducing the scan time via partial acquisition or parallel imaging have been proposed as a solution, a robust and yet simple to implement remedy still remains to be proposed. This work investigates the application of partial K-Space acquisition/completion methods to correct for motion induced artifacts occurring in MR images of the abdomen; if feasible, the application of such methods to motion correction permits for the amelioration of the artifact ridden image, without a great deal of additional burdens in the clinical application of the imaging.

Our study uses the mDIXON breath-hold sequence to image an abdomen phantom mounted on an MRI compatible motion platform, programmed by trajectories that mimic undesirable common motions such as coughs/hick-ups, constant inhale and exhale that often occur during breath-hold scans. By performing a parametric study of the resulting artifact to the parameters that characterize the programmed motion trajectory, we categorize the motion artifact in terms of the underlying motion that it originated from. A set of tools are then developed that permit for the manipulation, and correction of the K-Space and the resulting image. The developed set of tools provide a mechanism that permits for the study of the evolution of the image with the acquisition of the K-Space. Using our tools, regions in the K-Space that are acquired during the occurrence of the motion can be isolated, and manipulated to compensate for the motion. By applying our methodology to our experimental data obtained in the RTR 3T MR scanner, we show that even the simplest methods such as zero padding can lead to a reduction in the intensity of the observed artifacts, there-by permitting for an amelioration of the obtained image.

TABLE OF CONTENTS

ACKNOWLEDGEMENTS	ii
ABSTRACT	iii
LIST OF ILLUSTRATIONS	vii
LIST OF TABLES	xiv
Chapter	Page
1. Introduction	1
2. Theoretical Foundations	3
2.1 Magnetic Resonance Imaging	3
2.2 DIXON methods	6
2.3 K-Space	11
2.4 Parallel Imaging	14
2.5 Partial Fourier Techniques	24
2.6 Artifacts	26
2.6.1 Motion Induced Artifacts	27
2.7 A Review of Currently Available Methods to Reduce Respiratory Mo- tion Artifacts	28
2.7.1 Prospective methods	29
2.7.2 Retrospective Methods	31
3. Methodology	35
3.1 Experimental Setup	35
3.2 Motion Platform	39
3.3 Programmed Motion Trajectories	40

3.4	MRI sequence	47
3.5	K-Space Manipulation	50
3.6	Methods for K-Space Correction	51
3.6.1	Correction via zero padding	52
3.6.2	Correction via the conjugate symmetry rule	52
3.7	Data Analysis	53
4.	Results	59
4.1	First Set of Experiments	59
4.2	Second Set of Experiments	69
4.2.1	Motion before and after the center of K-Space acquisition . . .	70
4.2.2	Motion occurring during the scan and continuing to the end .	74
5.	Concluding Remarks	78
Appendix		
A.	MATLAB code for Raw Data Analysis tool	81
REFERENCES		94

LIST OF ILLUSTRATIONS

Figure	Page
<p>2.1 A two-point Dixon reconstruction of gradient echo data acquired on a 0.5 T scanner. Reproduced from [1]. Water image presents the water components while the fat image presents those of fat. However, there are parts, appearing as bright, in each of images corrupted by the presence of the other. This is caused by the off-resonance frequency ω across the head</p>	10
<p>2.2 The Cartesian acquired K-Space and its corresponding imageFOV. Reproduced from [2]; In the cartesian K-Space, the extent of K-Space that is acquired ($k_{x,max}$ and $k_{y,max}$) is inversely proportional to the image resolution. FOV in each direction is inversely proportional to the distance (Δkx and Δky) between the collected lines in K-Space</p>	15
<p>2.3 The impact of undersampling the K-Space on the Image. Reproduced from[2]; (a) For a full FOV, and a high-resolution image, it is necessary to acquire a fully sampled K-Space with the distance between phases satisfying the $\frac{1}{FOV}$ (b) By decreasing $k_{y,max}$, the resolution of the image is reduced (c) increasing the distance between frequency encoding lines maintains image resolution while reducing scan time</p>	16

2.4 Demonstration of SENSE. Reproduced from[3]; (a) Image of a phantom obtained. (b) image obtained from receiver coils 1 and 2. The arrow heads (triangles) highlight regions closer to the receiver coil, and therefore appear as bright in the image. The arrow points shows the darker sides of the image, further away from the receiver coils. (c) image as obtained by coil 1: $s_{1,1}$ and $s_{1,2}$ denote the signal intensities at locations 1 and 2 in the image reconstructed from coil 1. Points closer to coil 1 $s_{1,1}$ will appear brighter than those further away such as $s_{1,2}$. (d) image as obtained by coil 2: points closer to coil 2 $s_{2,2}$ will appear brighter than those further away $s_{2,1}$. (e) reconstructed image from the under-sampled K-Space for coil 1. a_1 in this image corresponds to the point $s_{1,1}$ in panel c). As a result of wrapping due to under-sampling the K-Space, the spatial location is reported falsely. (f) reconstructed image from the under-sampled K-Space for coil 2. a_2 represents the point $s_{2,1}$ in panel (d). (g) two points on the phantom, with unknown intensities p_1 and p_2 . (h) SENSE reconstructed image. (i) intensity corrected image 20

2.5 Convolution rule for the GRAPPA algorithm. Reproduced from[2]. The first row corresponds to the image domain. Multiplication of a fully sampled K-Space image by the corresponding coil sensitivity profile (middle) will result in a single coil image(right). The corresponding K-Space is shown in the second row. The same relationship is found, with the convolution of the first (object) with the coil sensitivity K-Space (middle), giving single-coil k-space. As observed (right), many of the points are affected by the coil sensitivity 22

2.6	The GRAPPA reconstruction scheme. (a) the under-sampled K-Space acquired by each coil is presented in a different color. The dotted black box is a set of data points including some targets (empty circles) and some source points (solid dots) that shows the combination of data points from K-Spaces in which GRAPPA reconstruction acts. (b): auto-calibration signals (ACS) acquired near the center of the K-Space. (c) The kernel passes through the ACS regions of each coil to calculate the GRAPPA weights. (d) Calculated weights are used to estimate the target points. The final K-Space would be fully sampled. (e) Multiple channel images then are combined to create a full FOV image	34
3.1	Layout of the motion platform as secured to the MRI couch	37
3.2	Motion platform with the abdomen phantom mounted on it. The phantom is secured with the rubber bands in order to avoid unwanted motion of the phantom during the data acquisition process	38
3.3	Motion platform with phantom and the body coil; the body coil includes 32 RF channels and sits on top of the phantom to provide a multichannel MR scan. The set up is ready for undergoing the data acquisition . . .	39
3.4	The general sinusoidal wave trajectory and its characteristic variables .	42
3.5	Attempted trajectories for the first set of experiments; first two rows are the trajectories that last for three seconds and occur at start (first column), in the middle (second column) and at the end (last column) of the data acquisition process; amplitudes are respectively 1 and 2 cm for the first and second rows. Third and fourth rows have the same order, while the duration of the motion is extended to 6 seconds. The last row presents drift failures with amplitude of 1 cm (left) and 2 cm (right) .	44

3.6	Trajectories for the second set of experiments; (a) and (b) are one sharp sinusoidal wave before (a) and after (b) the center of K-Space; the second row shows the trajectories with motion starting during the scan and continuing until the end. Panel (c) has the most corrupted data between, and (d) has the motion occur after the center of K-Space. Panel (e) has the least corrupted data and results in an image similar to the stationary scan	46
3.7	Indices for K-y and K-z acquisition; (a) shows K_y points being acquired as a function of the scan time, (b) represents how K_z are acquired from minimum number 1 k_z point to maximum number of 71 k_z points. Not all K_z points are acquired for every K_y and this makes processing more difficult; K_x plane is composed of 456 points, acquired simultaneously meaning that for every single point in K_z graph (b) there are 456 points in frequency encoding direction that are filled almost at the same time, (c) Depicts one of the lines of K_z from (b) to make it easier to understand the way each k_z line is acquired	49
3.8	Reproduced from ' http://mriquestions.com/field-of-view-fov.html '; The distance between two entries of a 2D K-Space (here Δk) is inversely related to the extent of FOV and pixel size (Δw) and from symmetry considerations an inverse relation exist between $k_{FOV}(= 2K_{x,max})$ and spatial resolution (pixel size) in image domain (Δw). The K-Space, and image are assumed to be quadrangular meaning $FOV_x = FOV_y = FOV$ and $\Delta x = \Delta y = \Delta w$	50

3.9	Coil averaged image vs. scanner reconstructed DICOM: simple averaging over coils does not lead to a reasonable image (first row); a guess image is defined and weighting factors are assigned to each coil defined using the error of the coil image and the guess image. Channels with a lower error are given a higher weighting. The image at the bottom is the scanner reconstructed image to be compared with the result of our simplified version	57
3.10	Flow chart for processing and correcting the raw data	58
4.1	Contribution of the central and periphery of the K-Space to the final image. Presented in each row are the K-Space, the corresponding image, its error with the reference/stationary image, and the reference image. The top row corresponds to the image obtained after the removal of the center of K-Space and the bottom row corresponds to the image obtained after removal of the periphery of the K-Space	61
4.2	Comparison of the motion artifacts due to motion occurring at the start, middle and end of the scan. The first column presents the final image (first row) and the associated error due to occurrence of motion at the start of the scan. The column presents the final image and its associated error due to the motion occurring at the middle of the scan, and the last column corresponds to the final image and its associated error due to motion occurring at the end of the scan	63

4.3	Impact of the duration of motion on the motion artifact. The first column represents the final image (first row) and its error with the stationary (second row) due to a 3 seconds trajectory occurring at the start of the scan. The second column presents the final image and its error occurring at the middle of the scan. The last column presents the final image and its error due to a motion consistent over the entire duration of the scan	65
4.4	Comparison of motion artifacts for drifts of 1 cm and 2 cm respectively. Presented in the first column are the final image and the error for a 1 cm drift. The second column presents the final image and its error for a 2 cm drift	66
4.5	Regions of interest in the phantom. ROI 1 contains homogeneous tissue for two organs, including their boundary. ROI 2 contains homogeneous tissue representing a single organ. ROI 3 is composed of fat with the largest level of ringing observed in the previous figures	67
4.6	Comparison of motion artifacts for motion occurring before and after the middle of the scan time. Top row presents the image and the corresponding K-Space obtained from the motion trajectory (red) occurring prior to the middle of the scan. The bottom row presents the image and its corresponding K-Space as obtained from the motion trajectory after the middle of the scan	71
4.7	Correction multiplier and the corrected K-Spaces. Presented in the figure are the K-Space corrupted by motion, the zero-padded K-Space and their respective errors with the K-Space of the stationary image .	72

4.8	Comparison of the image prior to zero padding and after zero padding. Top row presents images corresponding to motion occurring prior to the center of the scan. Bottom row presents Reconstructed images after the center of the scan. Presented in each row are the artifact ridden image, the corrected/zero padded image, and their respective errors with the stationary profile as well as the corrected K-Space	73
4.9	K-Space and final image for motion that occurs near the start of the scan and continues well until the end. The first row presents the corrupted K-Space, the zero padded K-Space and their errors with respect to the stationary reference. The second row presents images corresponding to the K-Spaces presented in the first row	75
4.10	K-Space and final image for motion that occurs at the middle of the the scan and continues well until the end. The first row presents the corrupted K-Space, the zero padded K-Space and their errors with respect to the stationary reference. The second row presents images corresponding to the K-Spaces presented in the first row	76
4.11	K-Space and final image for motion that occurs near the end of the scan of the the scan and continues well until the end. The first row presents the corrupted K-Space, the zero padded K-Space and their errors with respect to the stationary reference. The second row presents images corresponding to the K-Spaces presented in the first row	77

LIST OF TABLES

Table		Page
3.1	The sequence properties input for m-DIXON-W-BH SENSE. We note that the scan mode we have used is in 3D and spans 131 slices permitting for a FOV of 400x229x229 voxels after zero filling.	48
4.1	RMSE of the object image with respect to the reference stationary. ϵ_{SS} represents the background noise and is computed as the RMSE of two measurements of the stationary phantom. $\epsilon_{A,T}$ represents the RMSE of the image obtained from motion of amplitude A (in cm) at time T (in s). ϵ_A represents the drift of intensity A occurring at time T . The RMSE has been calculated according to $RMSE = \frac{1}{m \cdot n} \sqrt{\sum_{i=1}^{M-1} \sum_{j=1}^{N-1} [I_{ij} - I_{s,(i,j)}^2]^2}$ with M, N are the number of pixels in the X and Y direction respectively, and $I_{s,(i,j)}$ representing the stationary reference image.	68

CHAPTER 1

Introduction

Aside from the numerous advances in hardware and software for Magnetic Resonance Imaging, motion artifacts are still among the main obstacles to be overcome in order to acquire a well qualified image. A plethora of strategies aim at addressing this issue, with each method having its own weakness; for example, gated and triggering scans [4] integrate information regarding the motion into the acquisition system. While such strategies are promising, they also tend to result in long acquisition times, with protocols either being too sensitive to noise, or prone to shallow breathing errors. Complex sequence designs involving complicated acquisition techniques such as spiral K-Space [5][6], present an elegant way to capture and integrate information regarding the motion into the scan acquisition and post-processing. However, such methods are fundamentally challenging and currently outside of day to day clinical applications. Signal averaging [6] presents another approach leading to higher SNRs via acquisition and averaging of several data sets. While such methods may yield improvements when imaging large structures with little motion, a detailed structure that moves periodically or continuously will be averaged out or distorted in the final image.

By accelerating the data acquisition process, fast imaging attempts to complete the scan prior to the occurrence of motion in the region of interest. Breath-hold scans present one such acquisition strategy [7] [8] [9] [10]. Here, under ideal circumstances, the patient is educated to hold his breath while performing the scan. Success of such an approach relies heavily on the patient's ability to control his breathing, and

presents a difficulty for many individuals [11]. Suppression of the signal from the type of tissue (water or fat) with the largest motion associated with it would also have an additional positive impact on reducing motion artifacts. This is the strategy behind the mDIXON breath-hold sequences that are employed in this report to study motion artifacts in MR images of the abdomen [12] [1][6].

This study investigates the possibility for the reduction of motion artifacts in MR images as applied to tumor detection in the abdomen. This work has involved several hours of measurement at the RTR MR Scanner at UTSW, and the development of a set of tools in MATLAB for the analysis, manipulation, reconstruction and correction of scanner raw data. We use an MRI abdomen phantom, coupled with an MRI compatible motion platform [13], to simulate and study the various motion artifacts that arise from types of motions in common to breath-hold scans. By studying the artifacts that appear in the corrupted images, we attempt to classify the resulting artifact in terms of the underlying type of motion that it originated from. Once the type of artifact has been identified, we attempt to reduce the impact of the resulting artifacts in the final image via manipulation of the K-space.

This study is structured as follows: chapter 2 presents the underlying theoretical foundations including a brief overview of the MRI concepts and methods that the rest of this study is built upon. We then proceed to present our experimental methodology in chapter 3, and our approach for studying and correcting the motion artifact. Chapter 4 presents some of our results from two of our experiments. We summarize our results in Chapter 5 and present extensions and future avenues of research for our work.

CHAPTER 2

Theoretical Foundations

Magnetic resonance imaging provides a superb contrast of the various structures while giving no dose to the patient. The variation between tissue properties such as T1, T2 and proton density is what is being measured with MRI and what provides a great variety of contrast in the final image. Scan parameters such as repetition time, echo time, and flip angle, can be manipulated to suppress or enhance the contribution of a tissue parameter based on the desired clinical or research goal of the final image. Sequence design arises from manipulation of such parameters to address a certain goal. This study uses an MR sequence (m-DIXON BH-W SENSE) created to investigate the effect of respiratory induced organ motion in MR images of the abdomen. In this chapter, we advance towards a presentation of such a sequence by covering some of the underlying theory behind MRI and the K-Space, as well as common imaging techniques such as parallel imaging and DIXON methods. We will then discuss motion induced artifacts in MRI, and the various techniques (including methods and sequences) that aim to correct for it. Such techniques are used in the subsequent chapter to analyze our experimental results which are presented in chapter 4.

2.1 Magnetic Resonance Imaging

Magnetic Resonance Imaging is based on quantum mechanics and should therefore be explained using quantum mechanical notions. Signals arising from the energy exchange between nucleons and a rotating electromagnetic field at a certain frequency

are emitted from the nuclei and used to generate an image; when particles of non-zero spin are placed in a strong external magnetic field, due to the spin angular momentum, their spins tend to align in the direction parallel or anti-parallel to the applied magnetic field. When an RF pulse at the larmor frequency (the frequency of rotation of the spins) is applied, the spin of each particle is forced out of perfect alignment and the population of the spins begins to rotate in a cone-shaped trajectory. The Gyro magnetic ratio γ is a parameter unique to each nuclei and determines the shape of this trajectory. The Gyro-magnetic ratio (magnetogyric ratio) is related to the spin angular momentum as well as the rate of precessing around the external magnetic field by :

$$\mu = \gamma S \quad (2.1)$$

Or

$$\nu = \gamma B \quad (2.2)$$

where the spin S and magnetic moment μ are collinear and directly proportional to one another and the gyro-magnetic ratio γ . When placed in a magnetic field with strength B , a particle with a net spin can absorb a photon of frequency ν . The frequency ν depends on the gyromagnetic ratio γ of the particle. For hydrogen, $\gamma = 42.58MHz/T$.

T1 relaxation time, also referred to as spin-lattice relaxation time, is a way to measure how fast the longitudinal magnetization loses it's energy to the neighboring nuclei (lattice) and returns to it's ground state [14]. This growth of net magnetization is governed by a time constant that describes the time required to recover 63 percent of the signal. After about three to five T1s, the signal is approximately recovered. This time is related to the amount of lattice structure that exist in the tissue and the

likelihood of energy exchange between the spins and the lattice.

T2 relaxation time is the transverse relaxation that describes the progressive dephasing of the micro dipoles following the 90 degree RF pulse. This occurs much faster than T1 relaxation, and is easier to measure. It can be measured by reading out the receiver coil at different times, and plotting the curve connecting them described by an exponential decay. T2 describes the amount of time that is required to have 37 percent of the initial transverse magnetization; it is different for each tissue and depends on the transfer of energy from spins in the higher energy state to those in the lower energy state. T1 and T2 are independent from each other as T1 describes the transfer of energy to the lattice while T2 describes the loss of coherent nuclear spins due to spin-spin interaction or field inhomogeneities [15].

A common property of some elements, also called zero spins, is that they do not have an equal number of protons and neutrons in their nuclei. NMR only works for such isotopes, with the preference given to those of higher abundance for easier detection [16]. Hydrogen is one such elements whose properties make it ideal for MR imaging. As a result, we often tend to look at water because of it's abundance in the body and also because the high strength of the proton signals in the H₂O molecule tends to generate more accurate images.

The goal of an MRI scan is to differentiate the different structures, and observe abnormalities. Hence, the image contrast is set according to the observed abnormality. By varying scan parameters, MR sequences try to emphasize/highlight certain contrast characteristics of the anatomical structure of interest. Primarily, tissue density determines the contrast. However, scanning parameters such as the Echo time

and the repetition time also plays an important role and can be varied to obtain better results. Varying these parameters is a widely used technique for defining MRI pulse sequences. In MR terms, by choosing a short TE and a long TR, the obtained image will represent the proton density of the tissues so that T1 and T2 relaxation effects are minimized. A T2-weighted imaging (here the T1 relaxation effects are minimized), has a long TR and a short TE. This results in the water parts of tissue to appear bright on the image while tissues with high amount of fat appear as dark. Since most lesions are associated with water, this approach is helpful in demonstrating pathologies. On the other hand, T1 weighted imaging minimizes the effect of T2 by having a short TR and a short TE. Tissues with high fat content appear bright while ones with water appear as dark; this is useful when one wishes to represent the anatomy of the body.

While such approaches are useful for many applications, they can not fully cover the necessity for separation of water and fat in MR imaging. Since we require water signals to be represented in the image more clearly than fat, separation of fat and water is important for diagnosis, [17]. However, fat signal often appears as bright in most types of images. The need for a method that can separate water and fat has led to the design of other sequences and methods. DIXON methods [18] are one group of such methods used in this study and are described in the next section.

2.2 DIXON methods

As mentioned in the previous section, fat has a short T1 so that it appears bright on most types of MR images. This is particularly true for T1 weighted images where the echo time is long enough for the signal to decay considerably. The bright appearance of fat can obscure the water parts of the body in the image. However,

this is not desirable due to importance of water in medical diagnosis; for example, tumors often appear as bright as fat in MR images, which can result in them being mistaken for fat tissue. Therefore, separating fat and water regions from one another has been a subject of great study.

A number of methods have been developed for separating water and fat regions. The majority of existing methods are based on either chemical shift or the short T1 of fat. Two examples of such methods are CHESS and STIR; Chemical Shift Selective Saturation (CHESS) is a widely used clinical method that tunes an RF pulse to the fat resonance frequency with a spoiler gradient saturator. This causes dephasing of fat protons and results in a signal produced from only water protons [19]. Short T1 Inversion Recovery (STIR) is based on the short T1 relaxation time of fat in comparison to almost all other tissues present in the body. STIR tries to invert water and fat magnetization and applies a delay time to zero the fat longitudinal magnetization (due to its shorter T1). However, at the time of RF excitation, longitudinal magnetization of water is not zero and is the signal acquired by receiver coils. Therefore, the image is primarily acquired from water signal and not fat. However, while nulling fat magnetization, STIR also weakens the signal from other tissues. Additionally, unless additional adjustment is provided, STIR is also sensitive to B1 non-uniformity [20].

Another approach for separating water and fat is water excitation. Water excitation focuses on fat elimination and uses a short series of RF pulses to excite only water protons and create an image from water only; water excitation is widely used for the evaluation of cartilage musculoskeletal in the musculoskeletal system [21]. Spectroscopic methods can also be used to quantify the portions of fat and water in the imaged tissue. These methods aid in diagnosis as they permit to determine the rel-

ative proportionality of each material (such as fat and water) present in the imaged object.

A widely used set of methods which provide a melange of the above strategies to separate water and fat are DIXON methods. DIXON methods are widely used for abdomen imaging. These methods attempt to address the differences in water and fat resonance frequencies (chemical shift) using the adjustment of the echo time (TE). DIXON methods separate water and fat by creating in-phase and out-of-phase sets of images. They do this by by acquiring 2, 3 or more echoes (also called number of points in Dixon methods) at different TEs; mathematical operations are then applied to extract water only and fat only images.

Dixon [12] uses a two point method which is sensitive to inhomogeneity of B_0 , so that a small fluctuation in B_0 can result in a deprecated image. This strategy has been the basis for development of a series of methods in water and fat suppression methods in MRI with the modified versions of the DIXON method are less sensitive to B_0 and B_1 heterogeneity than CHESS/Fat-Sat methods. This work utilizes the multi-point DIXON method (mDIXON) which is available on the Philips 3T RTR scanner. The mechanisms of the mDIXON sequence are similar to 2P and 3P DIXON methods so that we will provide a quick survey of the theory behind these methods.

2.2.0.1 Initial two Point Dixon Method

In this method a linear combination of two images is used to distinguish water and fat regions. Assuming that only water and fat are present (see figure 2.2.0.1 [1]), the obtained image will have the form:

$$I = I_w + e^{-i\omega_f T E_i} I_f \quad (2.3)$$

where I_w is the water component, and I_f is the lipid/fat component in the obtained image I . If the echo-time $T_{E,i}$ is chosen such that its product with the larmor frequency ω_f is a multiple of π , i.e. $T_E \omega_f \in [2n, (2m+1)\pi, 2\pi]$ for $n, m \in \mathbb{Z}$, then the two images will have the form:

$$I_1 = I_w + I_f \quad (2.4)$$

$$I_2 = I_w - I_f \quad (2.5)$$

$$(2.6)$$

As a result, the water and fat components I_w and I_f can be extracted by subtraction so that:

$$I_w = \frac{1}{2}(I_1 + I_2) \quad (2.7)$$

$$I_f = \frac{1}{2}(I_1 - I_2) \quad (2.8)$$

$$(2.9)$$

A basic problem that arises from the assumption that the image has the form given by equation 2.10 is shown in the white highlighted region outlined in figure 2.2.0.1. Here, we see a non-water, non-fat region that appears in both images due to the off-resonance frequency ω in the head. Three point Dixon methods try to address this problem by using three linear combinations of the components I_w and I_f .

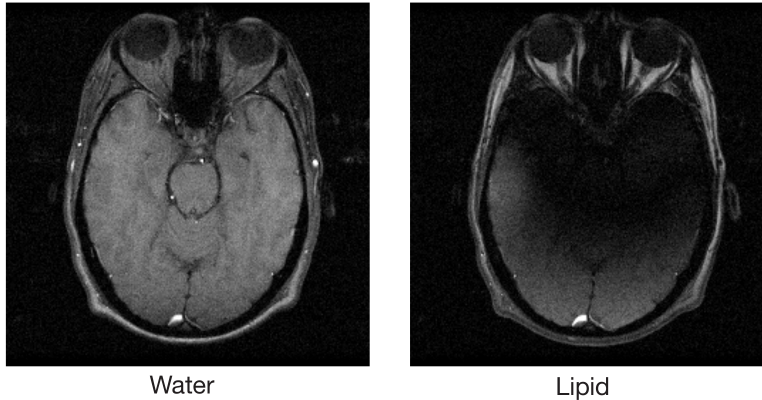


Figure 2.1. A two-point Dixon reconstruction of gradient echo data acquired on a 0.5 T scanner. Reproduced from [1]. Water image presents the water components while the fat image presents those of fat. However, there are parts, appearing as bright, in each of images corrupted by the presence of the other. This is caused by the off-resonance frequency ω across the head.

2.2.0.2 Three Point Dixon Methods

Three point Dixon methods attempt to account for the off-resonance frequency by introducing a phase term ϕ . Three images I_1 , I_2 and I_3 , taken at intervals of $\omega T_E, i = 0, \pi, 2\pi$, will have the form:

$$I_1 = I_w + I_f \quad (2.10)$$

$$I_2 = (I_w - I_f)e^{i\phi} \quad (2.11)$$

$$I_3 = (I_w + I_f)e^{2i\phi} \quad (2.12)$$

The phase corrected image is then given by[1]:

$$\hat{I}_w = \frac{1}{2}((I_w(1 + e^{i\phi}) + I_f(1 - e^{i\phi}))) \quad (2.13)$$

Symmetrically acquired echoes in three-point -DIXON cause a certain type of artifact that are addressed in a study by Reeder and colleagues [22] who introduced

IDEAL (Iterative Decomposition of Water and Fat With Echo Asymmetry and Least-Squares Estimation), and claim that the noise performance on any water-fat separation method is a function of the proportion of water and fat in any given voxel and the relative position of acquired echoes to the spin echo. They have modified the three point DIXON to perform an optimization for the phase encoding gradients. Their technique uses alternative water/fat phase-encoding strategies. This multi-point method has different phase encoding values than three point to overcome optimization issues in the three point-DIXON and also gives the user the chance of measuring spectral width of the fat resonance [23]. This method has lower SNR in comparison to three-point DIXON, at the cost of longer scan times.

2.3 K-Space

K-Space is an array of collected signals representing spatial frequencies, with radio-frequency pulses being responsible for their generation. Each entry is a data point from the scanner with its value (it's brightness) representing the relative contribution of spatial frequency of that entry to the final image.

Although the K-Space and it's corresponding MR image look very different, all the information of the acquired image is included in K-Space. The resolution of the image, FOV and even the time duration of the scan can be determined from exploring the K-Space. It is possible to reduce the scan time by reducing the total number of acquired points in the K-Space [24] (more effectively in the phase encoding direction).

The K-Space is presented in a format similar to figure 3.4. The k_x and k_y axes of the K-Space correspond to the horizontal (x) and vertical (y) axes in the figure. However, unlike an image which reports pixel intensities as function coordinates, the

K-Space reports amplitudes of the spatial frequencies in the x and y directions. Accordingly, a point in the K-Space does not correspond to its counterpart pixel (x,y) in the image domain; instead, it contains the spatial frequency and phase information related to every pixel in the final image domain. Conversely, each pixel in the image domain is related to all the points in K-Space.

Graphically, high frequency amplitudes are assigned to the outer edges in the K-Space while those for lower frequencies are found near the center. Accurate reconstruction and presentation of the image requires a good knowledge of the lower frequencies amplitudes. Hence, the center of the K-Space contains the most significant information regarding the image.

2.3.0.3 K-Space Structure

The study of MR motion artifacts and the manipulation of K-Space requires certain terminology which we will now describe to permit for a better understanding of the subsequent sections of this study.

Imaging a 3D subject involves encoding frequency amplitudes and phases over three directions (dimensions); the frequency encoding direction and the first and the second phase encoding directions. The frequency encoding direction is acquired in one repetition time (TR) by using an additional magnetic field gradient that slightly distorts the main magnetic field (B_0). The slope of the distortion is later used for spatial encoding in the direction of the distortion. The encoding works by relating the resonance frequency to image pixel locations. In this study, this direction is defined to be the x-direction (in-plane localization). Therefore, lines of K-Space in the

x-direction are assigned to be the frequency encoding direction. The other two directions are deemed as the first and second phase encoding directions.

Each line in the frequency encoding direction consists of signal amplitudes measured at successive points in time following TE. Varying the phase encoding gradients before the start of the next TR will take us to the next line in phase encoding direction. This will be continued by each line, there-by adding a certain amount to the phase encoding gradient until the entire K-Space is completed. The result is a traceable phase change in K-Space lines that is used to encode in this direction.

2.3.0.4 Properties of the K-Space & Scan Time

Certain mathematical property of K-Space required it to have conjugate symmetry; i.e. two points along the diagonal and equidistant from the center are complex conjugates. As we will see, this is a property that we can use to try and correct for motion artifacts; if we have half of the K-Space, then theoretically we should be able to predict and calculate the other half.

Removing some of the lines in K-Space will result in a reduced scan time. Long scan times are one of the clinical problems of using MRI; parallel imaging methods are an ever increasingly used strategy to try and overcome this issue. By acquiring only a portion of the K-Space and using the coil sensitivity maps as an additional source of information, parallel imaging methods aim to reduce scan times. The next section will present several key methods of current use in parallel imaging.

2.4 Parallel Imaging

Parallel imaging is a commonly used imaging method to reduce scan acquisition times. In this method, the spatial location of receiver coils in relation to the subject and also the sensitivity maps of the coils are used as an extra piece of information for spatially localizing the MR signals either in image domain/time domain. By including this information during the spatial encoding, some of the K-Space lines in phase encoding direction can be omitted. Sensitivities of receiver coils are then used to assist covering for the missing information. This, in-turn can potentially result in a significant decrease in the image acquisition time at the price of SNR. From the hardware side of things, the main requirement is the need for a scanner with independent receiver coils and sources.

Two parallel imaging methods include SENSE and GRAPPA [11]. As described below, these methods aim to reconstruct an image from a partially acquired K-Space. The study of how this image reconstruction is performed is beneficial to our cause - correction for motion from a K-Space that contains partially corrupted sections due to motion. As a result, we provide a quick survey of parallel imaging methods. Additionally, learning about these different methods will permit us to have a better understanding of their advantages and disadvantages.

When the K-Space data is collected in a Cartesian grid (see figure 2.4), the extent of the acquired K-Space ($k_{x,max}$ and $k_{y,max}$) is inversely proportional to the image resolution. The distance between neighboring entries in the K-Space (Δk_x and Δk_y) is inversely proportional to the field of view (FOV_x and FOV_y); therefore, changing the distance between data points or varying the extent that the K-Space is

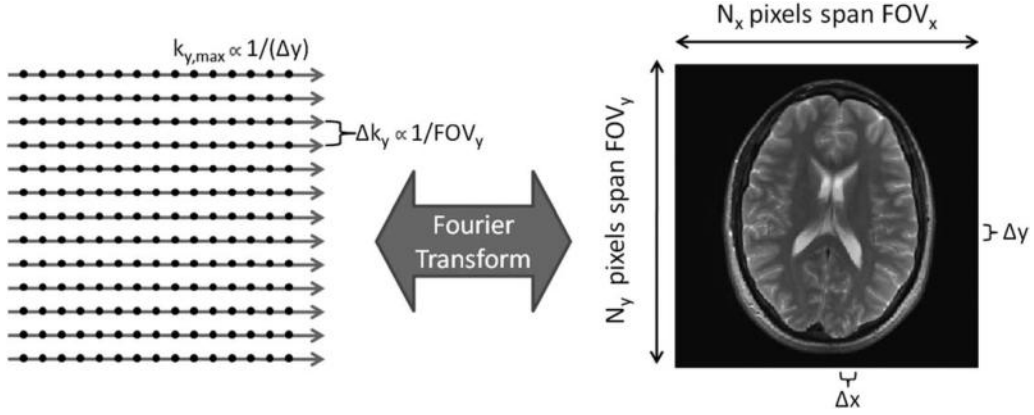


Figure 2.2. The Cartesian acquired K-Space and its corresponding imageFOV. Reproduced from [2]; In the cartesian K-Space, the extent of K-Space that is acquired ($k_{x,max}$ and $k_{y,max}$) is inversely proportional to the image resolution. FOV in each direction is inversely proportional to the distance (Δk_x and Δk_y) between the collected lines in K-Space.

acquired, will affect the FOV and resolution of the final image.

The lines of the cartesian K-Space are acquired one by one: first over the frequency encoding direction (k_x) and then over the phase encoding direction. In this study, the k_y is chosen as the first phase encoding direction (see 2.4 as an example in 2D). There is another phase encoding direction if the data acquisition is 3D [25]; this is chosen to be (k_z). The total time t_{total} required to acquire all data points in the 3D acquisition is given by:

$$t_{total} = TR_y * TR_z * N_{PE} \quad (2.14)$$

where TR_y is the repetition time needed to acquire one line of K-Space in the first phase encoding direction and TR_z is the repetition time for the second one; N_{PE} is the number of lines in phase encoding gradients.

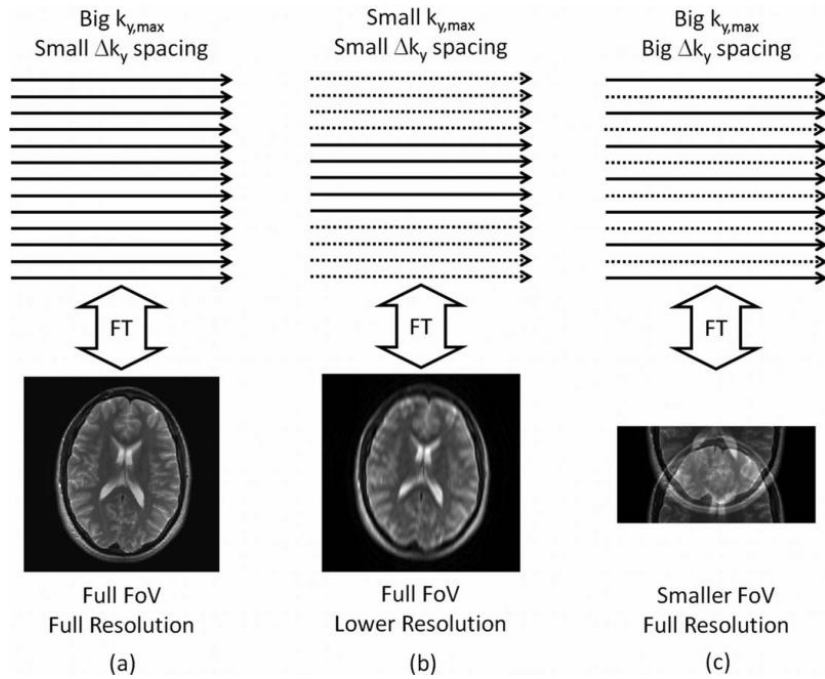


Figure 2.3. The impact of undersampling the K-Space on the Image. Reproduced from[2]; (a) For a full FOV, and a high-resolution image, it is necessary to acquire a fully sampled K-Space with the distance between phases satisfying the $\frac{1}{FOV}$ (b) By decreasing $k_{y,max}$, the resolution of the image is reduced (c) increasing the distance between frequency encoding lines maintains image resolution while reducing scan time.

Two ways to reduce the acquisition time are either by using a faster K-Space data collection (reducing the TR in equation 2.14) or by reducing the extent to which the K-Space is acquired (reducing N_{PE}). The speed at which K-Space data can be collected is adjusted based on the desired image contrast as well as the strength of the magnetic field gradients that are used to encode the K-Space data. Depending on the type of the scan and the sequence, different factors can limit the amount by which the the acquisition time can actually be reduced. For example, spin echo [26] already requires a long TR, so that a reduction in the acquisition time by reducing TR would be difficult, if not impossible. Another constraint encountered for reducing TR would be the possibility of inducing an electrical current in the patient's body or

the specific absorption rate (SAR) [27].

Another approach to reduce the total scan time is to acquire less data points in the K-Space, i.e. to reduce N_{PE} appearing in 2.14. Depending on which of the image properties is deemed as important, we can try reduce $k_{y,max}$ which in-turn lowers image resolution, or increase the spacing between the data points in K-Space by skipping some lines, which is equivalent to increasing Δk_y appearing in equation 2.4. This latter strategy results in a smaller FOV and aliasing or wrapping in the final image due to violation of the Nyquist criterion [2]. In this situation, the high frequency signal from one part of the subject is mixed with the low frequency signal from another part and the two parts are seen at the same point in the image. This occurs because the spacing between two consecutive points in K-Space is not small enough to make it possible to distinguish the frequencies from the different locations in the subject.

Addressing aliasing problems requires for the un-acquired sections of the K-Space to be encoded. Parallel imaging is used for this application and includes a large plethora of various methods. However, all of these methods have certain properties in common - the most obvious is the under-sampled K-Space in one or both of phase encoding directions, and an acceleration factor which dictates the proportion of lines removed.¹ Increasing this factor corresponds to reducing the scan time which results in additional aliasing in the image. The additional information needed for image reconstruction is extracted from each coils' position relative to the scanned object. Used algorithms accept the under-sampled data and coil sensitivity from each

¹For example, in this study, the sequence used is a 3D acquisition that has SENSE in both of its phase encoding directions. The acceleration factors are 1.5 and 0.5

individual coil as input and reconstruct the full FOV. Hence, multiple receiver coils are always used when reconstructing data using parallel imaging. The coil sensitivity describes just how sensitive a given channel is to any point on the subject's body and often varies from patient to patient. The sensitivity map of each coil should have as little overlap as possible with the other coils, and their sum should cover the FOV.

2.4.0.5 SENSE

SENSE is a parallel imaging method that corrects the aliasing in the image domain and not K-Space. The MR sequence we used in this project includes SENSE with acceleration factor of 1.5 in y-direction and 0.5 in z-direction; In SENSE, the Fourier transformation of the acquired, under-sampled, K-SPACE is performed and the aliased images are generated [28]. Then, coil sensitivity profiles are used to reconstruct the unwrapped images. With the SENSE method, the homogeneity and non-overlap of the coil sensitivity maps is not an issue; rather, the maps should be available before starting the reconstruction process. Usually a low resolution pre-scan is performed to collect this information [29].

Two rules are to be considered when using SENSE [3]:

- $k_{y,max}$ is important in determining the spatial resolution in the phase encoding direction with higher numbers of sampled points (N_y) resulting in a higher spatial resolution along the phase encoding direction.
- the spacing between data points in the phase encoding Δk_y determines the corresponding FOVs in the image domain.

In SENSE, aliasing artifacts are addressed using the spatial sensitivity profile for each coil element. The image is then a combination of each individual chan-

nel's image. The sensitivity profile of each element in the phased array relates the difference between signal intensities in each coil to the spatial location of each pixel. The sensitivity for each coil is unique and varies for each pixel in the image domain [3].

In matrix notation (see figure 2.4.0.5), we can denote \mathbf{a} as the image pixel intensities before reconstruction/unwrapping, \mathbf{p} as the image pixel intensities in the un-aliased/reconstructed image (unwrapped), and \mathbf{s} as sensitivity maps for all the coils at each spatial location. Values in matrix \mathbf{a} are then related to \mathbf{p} and \mathbf{s} as [30]:

$$a_1 = s_{1,1} * p_1 + s_{1,2} * p_2 \quad (2.15)$$

$$a_2 = s_{2,1} * p_1 + s_{2,2} * p_2 \quad (2.16)$$

The pixel values \mathbf{p} determined from the coil sensitivity profiles are the unknowns of interest in the above equations, and can be obtained by inverting the sensitivity matrix \mathbf{s} so that:

$$\mathbf{p} = \mathbf{s}^{-1} \cdot \mathbf{a} \quad (2.17)$$

SENSE reconstruction maintains the same image contrast and spatial resolution as a standard scan, but in half of the acquisition time with a reduced SNR. The SENSE reduction factor can be as large as the number of coils. However, high reduction factors result in undesirably low SNRs so that a significantly lower value is typically used.

The total extent/size of acquired K-Space remains the same which maintains image resolution. However, the distance between adjacent k-space lines that are acquired is increased by a reduction factor R . So the signal from R locations, equally spaced along the sub-sampled direction, overlap in/wrap-around the image. Provided that the coil sensitivity is different at each pixel and for each coil, the weights given

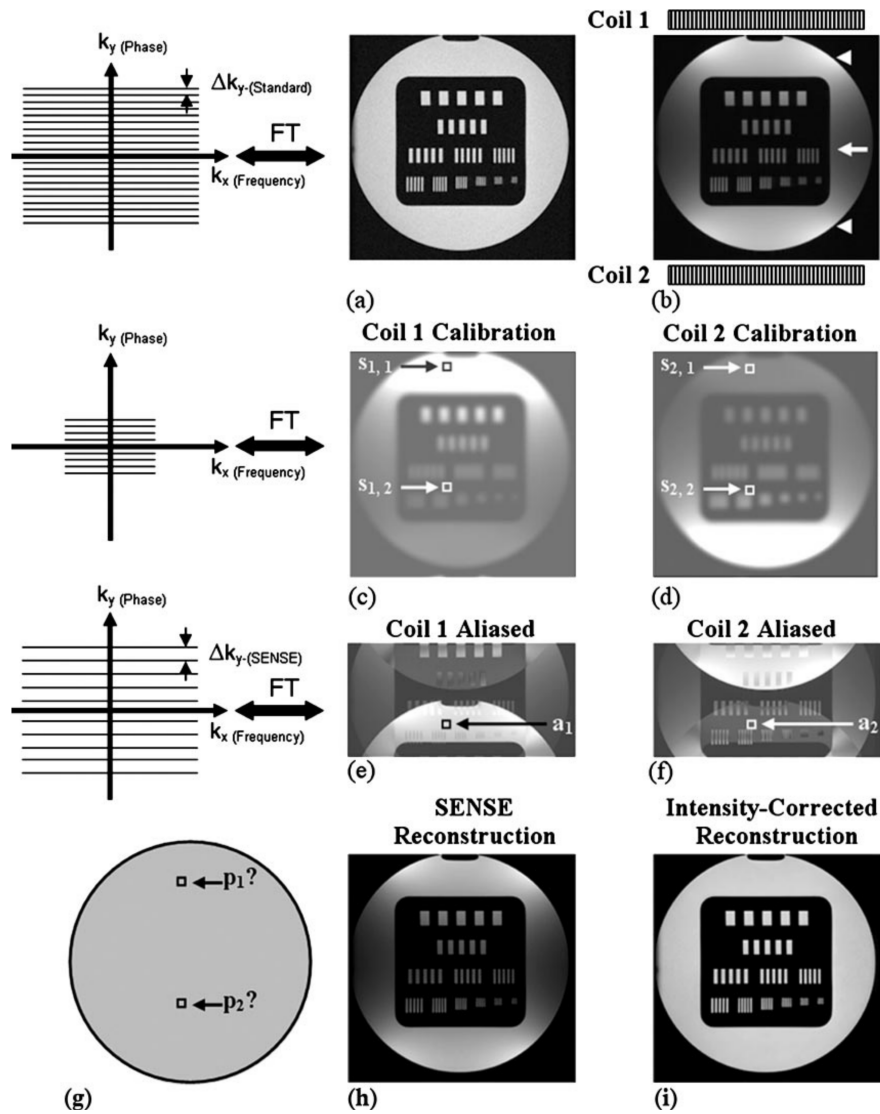


Figure 2.4. Demonstration of SENSE. Reproduced from [3]; (a) Image of a phantom obtained. (b) image obtained from receiver coils 1 and 2. The arrow heads (triangles) highlight regions closer to the receiver coil, and therefore appear as bright in the image. The arrow points shows the darker sides of the image, further away from the receiver coils. (c) image as obtained by coil 1: $s_{1,1}$ and $s_{1,2}$ denote the signal intensities at locations 1 and 2 in the image reconstructed from coil 1. Points closer to coil 1 $s_{1,1}$ will appear brighter than those further away such as $s_{1,2}$. (d) image as obtained by coil 2: points closer to coil 2 $s_{2,2}$ will appear brighter than those further away $s_{2,1}$. (e) reconstructed image from the under-sampled K-Space for coil 1. a_1 in this image corresponds to the point $s_{1,1}$ in panel c). As a result of wrapping due to under-sampling the K-Space, the spatial location is reported falsely. (f) reconstructed image from the under-sampled K-Space for coil 2. a_2 represents the point $s_{2,1}$ in panel (d). (g) two points on the phantom, with unknown intensities p_1 and p_2 . (h) SENSE reconstructed image. (i) intensity corrected image.

to the signal components will also vary (i.e. \mathbf{s}^{-1} exists). Finally, we note that the defined FOV should include the entire body part; otherwise, other parts out of FOV will also have aliasing that has not been accounted for.

2.4.0.6 SMASH

SiMultaneous Acquisition of Spatial Harmonics uses linear combinations of coils and benefits from sensitivity variations in the surface coil array to replace the missing information in the unacquired phase encoding lines. Sinusoidal spatial modulations, or 'spatial harmonics', are formed by linear combination of measured component coil sensitivities, and the same linear combinations are applied to component coil signals in order to generate shifted composite MR signals that can take the place of omitted gradient steps [31].

2.4.0.7 GRAPPA

GeneRalized Auto calibrating Partial Parallel Acquisition (GRAPPA) is a parallel imaging technique that samples only a limited number of phase-encoding steps [32]. GRAPPA is a type of SMASH, where a few more lines of the K-Space are obtained during the acquisition to eliminate the need for a separate coil sensitivity calibration. GRAPPA yields a better SNR than SMASH and eliminates certain associated artifacts [10]. In comparison to SENSE, GRAPPA corrects the K-Space prior to the application of the Fourier transform while SENSE uses the sensitivity maps as an additional piece of information to sort out signals in the image domain after a Fourier Transform.

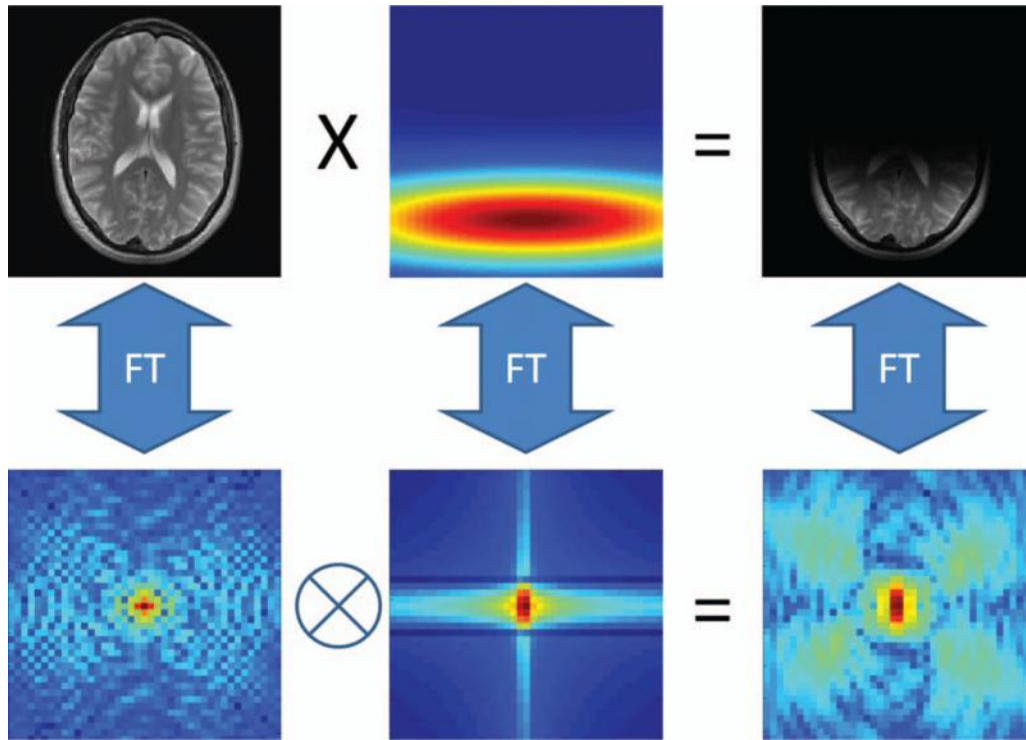


Figure 2.5. Convolution rule for the GRAPPA algorithm. Reproduced from[2]. The first row corresponds to the image domain. Multiplication of a fully sampled K-Space image by the corresponding coil sensitivity profile (middle) will result in a single coil image(right). The corresponding K-Space is shown in the second row. The same relationship is found, with the convolution of the first (object) with the coil sensitivity K-Space (middle), giving single-coil k-space. As observed (right), many of the points are affected by the coil sensitivity.

The correction to the K-Space is based on using the acquired portions of K-Space to predict the missing ones, with the assumption that information from any point in the K-Space can be extracted from its neighboring points. Figure 2.4.0.7 shows that the location of the coil affects all pixels by weighting them with the coil sensitivity profile. In the K-Space, this effect is seen by the distribution of this information over the neighboring data points.

The weighting factors in the GRAPPA algorithm are obtained by acquiring several extra lines of the K-SPACE and combining the acquired points to predict missing ones. The set of acquired points are called source points, while missing points are referred to as targets. The dotted black box appearing in figure 2.4.0.7 presents the kernel used to calculate the weights from ACS (auto-calibration signal) lines by finding the mathematical relationship between source and target points. This information is used to compute the value of the target points and reconstruct a complete K-Space for each of the coils. Correspondingly, several single-coil fully sampled K-Spaces are obtained, the combination of whom will create a full FOV image.

In parallel imaging the number of receiver channels in the coil array limits the maximum acceleration factor that can be used. Generally, the acceleration factor cannot be higher than the number of coils in the array. However, in practice, it is usually chosen to be much smaller to generate images of clinical quality. Although much higher gains are theoretically possible, parallel imaging increases the acquisition speed by a factors of 1.5 to 3 in most clinical MRI scanners; higher factors are currently limited by artifacts and signal-to-noise ratio (SNR) considerations. With parallel imaging, since there is less signal acquired, the sensitivity of the images from parallel imaging to signal loss due to gradient magnetic field dephasing is lower than regular scans. However, the SNR lowers as the acceleration factor grows higher so that an optimum acceleration factor must be chosen.

Unlike SENSE, GRAPPA does not solely rely on coil sensitivity profiles. This property results in a more robust algorithm in cases where measuring sensitivity maps is difficult. The number of ACS lines can change as well as the size of kernel which gives flexibility to the GRAPPA algorithm. Increasing the ACS size yields more ac-

curate weights at the price of longer scan times.

2.5 Partial Fourier Techniques

From the laws of Fourier transforms [33], we know that the K-Space is conjugate symmetric. This means that pairs of points located on a diagonal and equidistant from the center are complex conjugates of each other. Such two points are equal in amplitude but opposite in phase. Using the conjugate or Hermitian symmetry rule, and assuming that no phase error occurs during the data acquisition [8], only half of the K-space data points are required to create a complete 2D MR image. In MR terms, the signal intensity on the downward portion of a positive phase encode step echo is the conjugate complex of the downward portion of the corresponding echo acquired with a negative phase encoding step. The remaining half can be estimated from the complex conjugate of the corresponding acquired data points. Since only half of the data points in the K-Space are needed to reconstruct a well qualified image, it can be expected that the imaging time and/or the minimum echo time will be reduced.

While the ideal MR K-Space may be conjugate symmetric, MR images always have a certain level of phase error caused by B0 in-homogeneity, eddy current, motion or spatial variation in the RF transmit as well as sensitivity coil maps [10]. To overcome the phase error, extra points from the remaining half of the K-Space are also acquired and used to export the phase correction maps for each data set. How much of the K-Space is actually acquired varies from method to method. For example, in echo-planar imaging (EPI), echoes acquired after the RF-excitation pulse will have a different phase than those that occurred prior to the RF pulse. This introduces an additional source of phase errors which render error estimation difficult. For EPI,

often 6/8 to 7/8 of k-space must be sampled to accurately estimate the remaining portion [34]. Generally, a parameter known as Partial Fourier Fraction is used to define the ratio of the number of acquired data points to the total number of points in the entire/filled K-Space. The Partial Fourier Fraction defined for a half-Fourier acquisition would be 0.5; acquiring more points increases this number to 1 which is equal to the entire space.

The most common types of partial Fourier imaging available on clinical machines are [7]:

- **Phase Conjugate Symmetry (partial NEX)**: collects half of K-Space data points and estimates the other half in the phase encoding direction. The total number of phase encoding steps has been reduced which will have a direct impact on the scan time, reducing it up to 40 percent at the expense of Signal to Noise Ratio.
- **Read Conjugate Symmetry (partial echo)**: the K-Space is halved in the Frequency encoding direction and used to estimate the other half. With this method, there is not a great deal of scan saving; however, echo time is reduced. Additionally, this decreases gradient moments which can help reduce motion artifacts. Major applications of this method would be in use with echo-planar techniques for applications such as MR angiography and T1 weighted spin-echo imaging. Unlike phase conjugate symmetry, this method increases the SNR for a given TE. Additionally, it may accept smaller FOVs because of the lower gradient amplitudes for a longer sampling time for a given TE.

In all of the above methods, artifacts are still a major problem and pose an un-resolved issue for clinical and research MR use. As a result, there still remains the need for methods that attempt to address this issue. In this study, we attempt to investigate

methods which aim to correct for motion type artifacts via reconstructing a corrected K-Space.

2.6 Artifacts

Artifacts refer to disparities between the true object and the represented image. Such disparities could be the appearance or disappearance of regions, or geometric changes in the represented region. Recognizing artifacts requires an in-depth knowledge of the types of artifacts that one encounters. Therefore a good knowledge of artifacts is helpful in distinguishing them from pathologies (or vice versa).

Artifacts can be categorized based on their cause, some of which include [35],[36]:

- Radio Frequency off-set and quadrature ghost: Radio Frequency circuitry not detected successfully.
- Radio Frequency Noise: failure of the shielding.
- B0 in-homogeneity: the presence of metal objects near the B0 field.
- Susceptibility: variety of magnetic susceptibility of objects inside the field of view.
- Radio Frequency in-homogeneity: when the function of RF coils is interrupted, as would be by the presence of metal-like objects in the anatomy of subject.
- Chemical Shift: when the neighboring tissues have a large difference in chemical shift; specially important under large B0.
- Partial volume: when the voxel size is larger than the feature that we are interested in imaging.
- Wrapping: when the field of view is not chosen properly. This can occur in SENSE (a type of parallel imaging) and is fixed in the post processing, using the coil sensitivity maps (see section 2.4).

- Motion artifacts: motion in the partial or full image FOV
 - Bulk motion: occurs when the entire patient body moves, all the edges and margins change their place in the image.
 - Ghosting, blurring, ringing can all occur.

In this project, we attempt to correct for the corruptions/artifacts occurring in abdomen MR images arising from respiration induced motion.

2.6.1 Motion Induced Artifacts

Motion artifacts [37] occur when the object or part of it moves while being imaged. The motion results in inconsistencies in the K-Space data, and can cause different types of artifacts such as ghosting, blurring, and ringing. The time of the occurrence of the motion (with respect to the start of the scan time), and the duration of the motion affect the type and amount of inconsistencies in the K-Space. Such inconsistencies translate to the observed artifact in the acquired image. Some causes of motion induced artifacts are physiological motions such as cardiac motion, breathing and pulsation in the vascular system. These motions are also period and last for the entire duration of the scan. An example of a motion induced artifact is the ghosting lines in the K-Space that appear when the motion occurs during the entire acquisition. Additionally, if the motion passes through the entire object, then the resulting ghosting can be seen over the entire image as well. ²

The timing of the occurrence of the motion artifact also dictates some of its characteristics. For-example, when the motion occurs between the time of RF excitation to the time of echo collection (also called within view effect) blurring as well as an increase in the noise of the image are observed. This type of artifact is usually caused

²this type of motion artifact is also called view to view effect

by random motions in the subject such as swallowing or coughing. Such ringing type artifacts occur frequently, and can be due to small movements.

Although many studies have attempted to address the issue of motion artifacts, and a great number of techniques have been suggested, respiratory induced motion artifacts still remains a serious problems in clinical MR scans of the abdomen as well as chest. In the next section, we will provide a survey of some of the currently available methods which aim at addressing respiratory induced motion artifacts.

2.7 A Review of Currently Available Methods to Reduce Respiratory Motion Artifacts

One of the simplest ways to address respiration induced motion artifacts is to try and stop the motion from occurring during active periods of data acquisition. Particularly for MRI of the abdomen, a great deal of methods exist to suppress the artifacts caused by respiratory motion. Among these are: breath-hold scans, triggering and gating methods and compensation for respiratory motion. Such methods which aim at addressing object motion by changing/adapting the sequence are called prospective methods. A second group methods, also referred to as retrospective methods, try to aim at correcting for the motion induced artifacts in the post-processing/reconstruction step of the process. Below, we will provide a short summary of both categories.

2.7.1 Prospective methods

2.7.1.1 Breath-Hold Scans

One of the remedies for respiratory motion artifact in MR images is educating the patients to hold their breath during the scan time. The used MRI sequence is designed to satisfy the aim of having the most effective time of scan with the least possible respiratory motion. The scan time for these breath-hold sequences are usually adjusted to be less than 20-30 seconds. Breath-hold scans are one of the most effective ways to overcome respiratory motion artifact. Although they can lead to a significant improvement in the the quality of the image, there are still artifacts due to the patients' failure to hold their breath.

2.7.1.2 Triggering and gating methods

While the patient may not be able to hold his breath for the entire duration of the exam, breath-holding and triggering methods aim at synchronizing data acquisition with the motion of the subjects [38]. Triggering or gating methods aim to gate the sequence of image acquisition to the respiratory cycle of the object. One such example utilizes the scanner triggered with a simulator or sensor that starts the scan at the end of the exhale (tumor position is most stable), and stops during the breathing cycle (the respiratory motion is most prevalent), re-starting the simulation at the next end of subsequent exhales. Naturally, such methods will result in a longer scan times and additional un-comfort for the patient. Additionally, motion artifacts can still occur due to a slight drift in the patient as well as common cyclic low-depth breathing.

2.7.1.3 Compensation for respiratory motion

Image acquisition with compensation of respiratory motion uses the entire scan time productively; this method monitors the breathing cycle of the subject during the scan [39]. Parts of the K-Space that are more sensitive to motion are acquired during the R-wave (near exhale) in the respiratory cycle while less sensitive parts (which are high in amplitude phase) are acquired during the inhale and other parts of the respiratory cycle. Devices such as bellows help to reorder the phase encoding steps according to the patient's breathing cycle. Unlike the triggering example given above, the entire scan time is used effectively. However, like gating methods, artifacts arising from slight drift in patient position and cyclic low depth breathing still pose a problem.

While in most respiratory motion correction methods, information regarding the subject's breathing cycle is required, the above problems have resulted in much of the research in the past decade to lean towards utilizing direct methods for motion compensation in the respiratory cycles [40]. Examples of such methods include self-navigation and image based navigation [41].

2.7.1.4 Self navigation

The self navigation approach uses the data acquired from the scan to estimate respiratory motion. In this method, during the data acquisition process, the center line of the K-Space is repeatedly measured (at-least once per K-Space segment). This information is then used to detect and estimate the motion. Thesen and colleagues [42] outline a self-navigated approach applied to fMRI motion correction of the head. Their method leads to a significant decrease in the variance between successively ac-

quired datasets in comparison to other retrospective correction algorithms. However, these methods often involve complicated sequence design and are not widely available for the clinical use.

2.7.1.5 Image based navigation

An alternative approach to motion correction is to use real time images as the navigator. This is a prospective approach that will give us more options for motion corrections at the price of greater complexity and data processing. Image based acquisition functions by programming various sequence designs; one example of such a navigator is the three orthogonal two-dimensional spiral navigator acquisition, with a flexible image-based tracking method based on the extended Kalman filter algorithm for on-line motion measurement [5].

2.7.2 Retrospective Methods

The above methods all aim to lessen the impact of motion by changing/switching the data acquisition system (real-time) based on the available motion information. Such an approach is called the prospective correction. However, additional corrections for motion can be made to the acquired data upon completion of the data-acquisition process. Such post-scan post-processing methods are called retrospective correction for motion [37][5]. Retrospective correction permits for a more comfortable scan while more time and a greater degree of freedom is given to the data processing and reconstruction. Correction for non-linear motion is an option with such methods; however, this method prohibits adjustment of slice position caused by through plane movements so that through-plane type artifacts still remain a problem [43].

2.7.2.1 Cycle averaging

Another retrospective method that aims to correct for respiration induced motion is to perform scans over several breathing cycles and to average the obtained signal over various phases in the breathing cycle, hence reporting average phase representations of the image [44]. While such an approach leads to a higher SNR in the final image, it additionally increases the acquisition time in a stationary situation. Additionally, the obtained anatomy does not correspond to a real state of the patient's anatomy. Rather, it represents an anatomy, averaged over several respiratory cycles. Additionally, such methods require the use of external monitoring devices.

2.7.2.2 External monitoring methods

External monitoring devices such as respiratory bellows [45] or navigator belts can be used to study the patient's breathing pattern. However, their use often accompanies additional set-up times, and may not accurately reflect the motion in the volume of interest as they rely on external-internal motion surrogates. Finding an accurate external-internal surrogate model that relates the external anatomy to the changing internal anatomy is difficult and a current problem in RT [46].

If it was possible to effectively rely on the information obtained from external monitoring devices, and also avoid possible interpolation errors in the K-Space, then the information supplied from such devices could be effectively used to correct for the many different kinds of motion artifacts. However, use of such devices leads to a scope of problems for respiratory motion correction such as:

- when not well positioned, and also in case of irregular breathing patterns, scan times are likely to increase.
- if the variation in breathing trajectories is larger than expected, adaptive windowing techniques may not work. This leads to incomplete acquisitions.
- navigator monitors the surface motion. However, there are movements inside the body not visible on the surface. The actual motion may be in a different direction than what is monitored by the navigator.

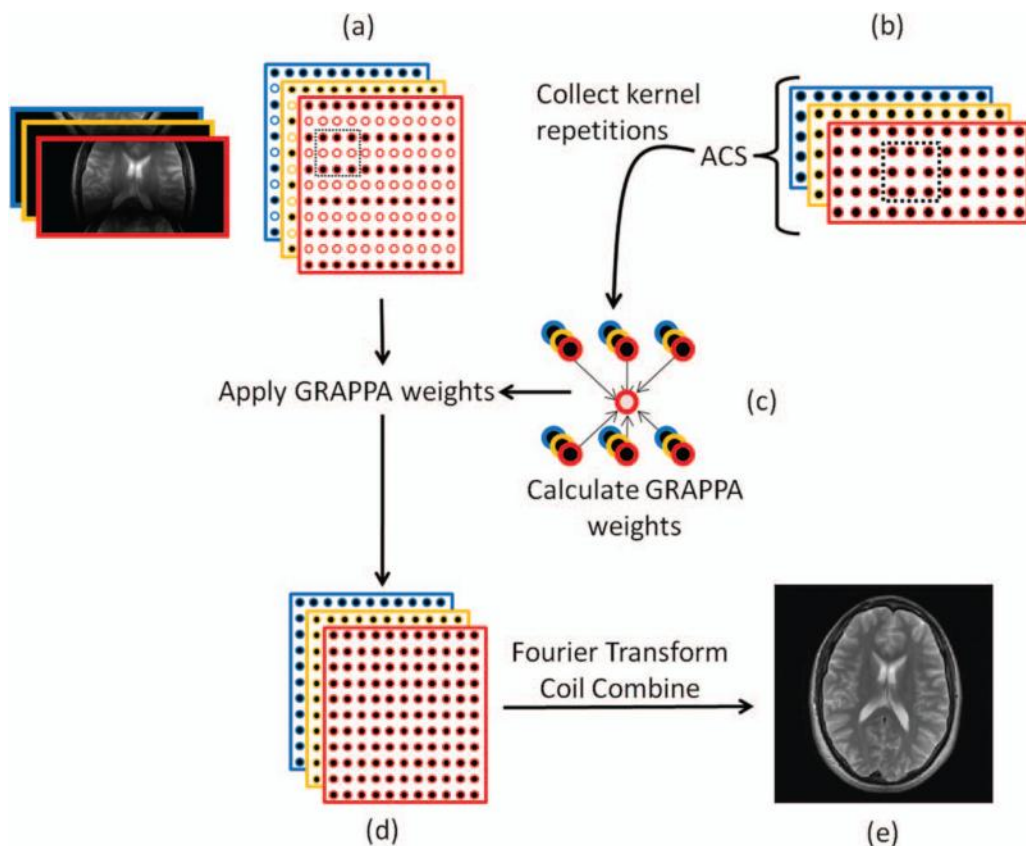


Figure 2.6. The GRAPPA reconstruction scheme. (a) the under-sampled K-Space acquired by each coil is presented in a different color. The dotted black box is a set of data points including some targets (empty circles) and some source points (solid dots) that shows the combination of data points from K-Spaces in which GRAPPA reconstruction acts. (b): auto-calibration signals (ACS) acquired near the center of the K-Space. (c) The kernel passes through the ACS regions of each coil to calculate the GRAPPA weights. (d) Calculated weights are used to estimate the target points. The final K-Space would be fully sampled. (e) Multiple channel images then are combined to create a full FOV image.

CHAPTER 3

Methodology

In this chapter, we outline our methodology for the two sets of experiments performed over the course of this study. The goal of these experiments is to investigate the possibility of correcting for the effect of motion artifacts by manipulating the K-Space. Naturally, in order to correct for something, we must first have a better understanding of its effect. Therefore, the first set of experiments were performed with the goal of studying the type of artifacts that arise from various types of motion trajectories; to do this, several sets of trajectories were programmed in an MRI-compatible motion platform coupled with an abdomen phantom, and MR scans were acquired using the mDIXON-BH sequence. Based on discussion of our results from this experiment with a trained MD/Physician, a second set of experiments with a similar set-up was performed to investigate the possibility of reducing the impact of the artifact in the final image. To analyze our data, a set of tools in matlab was developed that permit for the manipulation of raw data files exported from the scanner, their correction, and reconstruction of the final image. Our results pertaining to our experiments are presented in Chapter 4.

3.1 Experimental Setup

Our experiments were performed at the UTSW Radiology Translational Research (RTR) using a 3T MRI scanner (Philips, Ingenia). The experiments utilized an MR compatible motion platform coupled with an abdomen phantom. Three MRI

markers (vitamin E) are placed on the phantom. Since the markers are composed primarily of oil (lipid), they appear as bright spots in the image, thereby simplifying detection of their location. The first marker is placed in the superior direction of the phantom at the center. Another marker was placed on the left and inferior side of the phantom, and a third marker was placed on the inferior surface and up-anterior side of the phantom. Use of these markers permits to accurately determine the start and end of each plane, and aids in retrieving the locations in each plane during and after the movement of the phantom.

The trajectories, programmed into the motion platform, were chosen to represent motion in the abdomen due to a patient's failure to hold his breath during the breath-hold scan. The abdomen phantom that was used in these experiments includes organs such as the liver, kidneys, spinal chord, and is mounted on the motion platform so that its movement is synchronized with the motion platform (and hence the input trajectory). Figures 3.1, 3.2, and 3.3 present the experimental layout.

The procedure for experimental setup is as follows.

1. Set up the motion platform and test it before transporting it to the scanner room.
2. Compile and place all the trajectories at the required path and ensure that their duration is equal to that of the planned scan sequence. This step is crucial as using SENSE modifies the total acquisition time duration and should be taken into consideration while constructing the trajectories.
3. Place vitamin E pills/markers in the phantom at desired locations. Use of vitamin E simplifies detection in images.

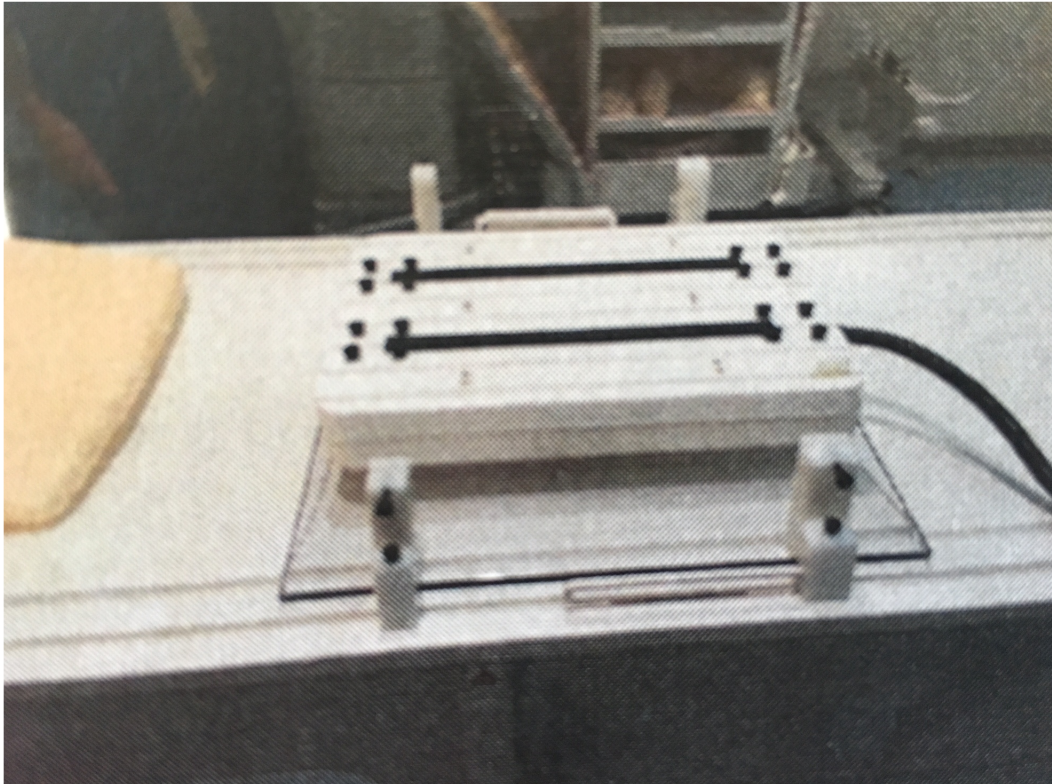


Figure 3.1. Layout of the motion platform as secured to the MRI couch.

4. Place the computer in the control room. The motion platform and phantom are placed in the MR room and secured on the couch.
5. Place a torso 32 channel RF coil over the phantom on the plastic spacer covering the phantom, with the phantom placed under the center of the body coil.
6. Set the iso-center at the correct location.
7. run the m-DIXON-W-SENSE sequence on the scanner specifically designed for this study at the RTR 3T scanner.

-in the first set of experiments, SENSE is on and data is exported in par rec format.

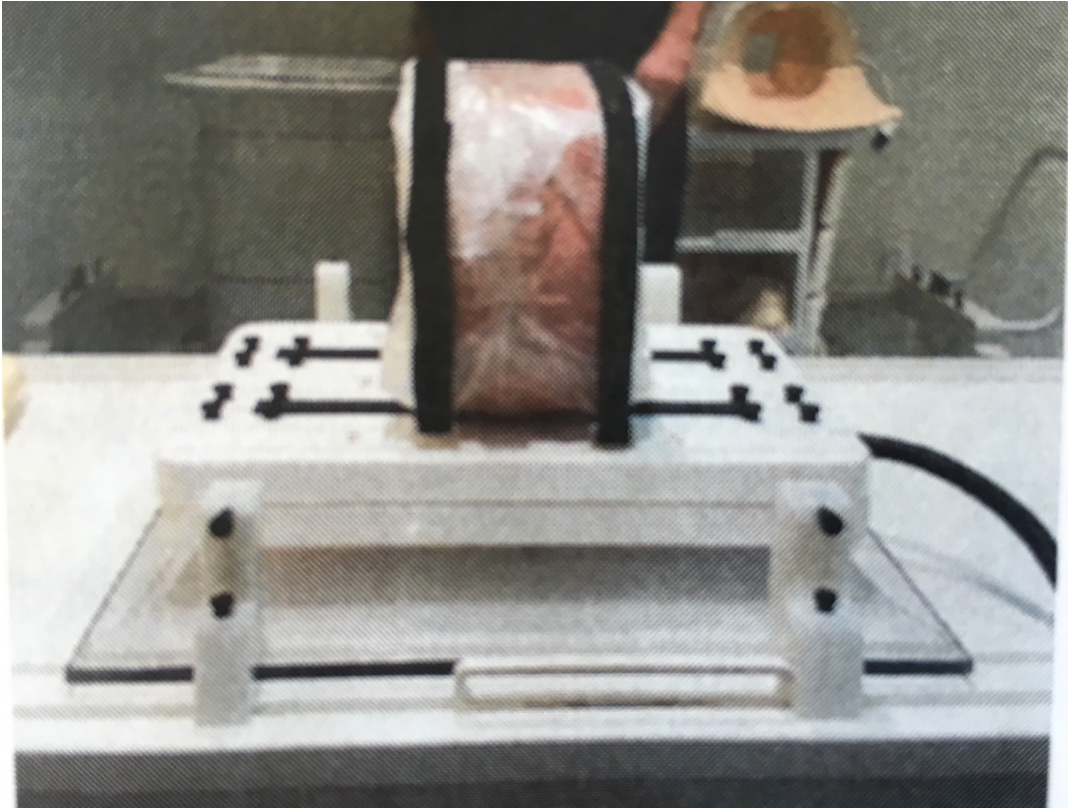


Figure 3.2. Motion platform with the abdomen phantom mounted on it. The phantom is secured with the rubber bands in order to avoid unwanted motion of the phantom during the data acquisition process.

-in the second set of experiments, scanner reconstruction is turned off and the raw data (format .RAW and .LIST) are exported. Additionally, scanner reconstructed DICOM files are also exported for validation.

The above procedures require at least 30 minutes to complete.

One of the questions that we aim to investigate in these experiments is how the intensity of the artifact changes with respect to variations in the amplitude and duration of the motion. For this reason, we have carefully selected and programmed several trajectories with different properties into an MRI compatible motion platform.

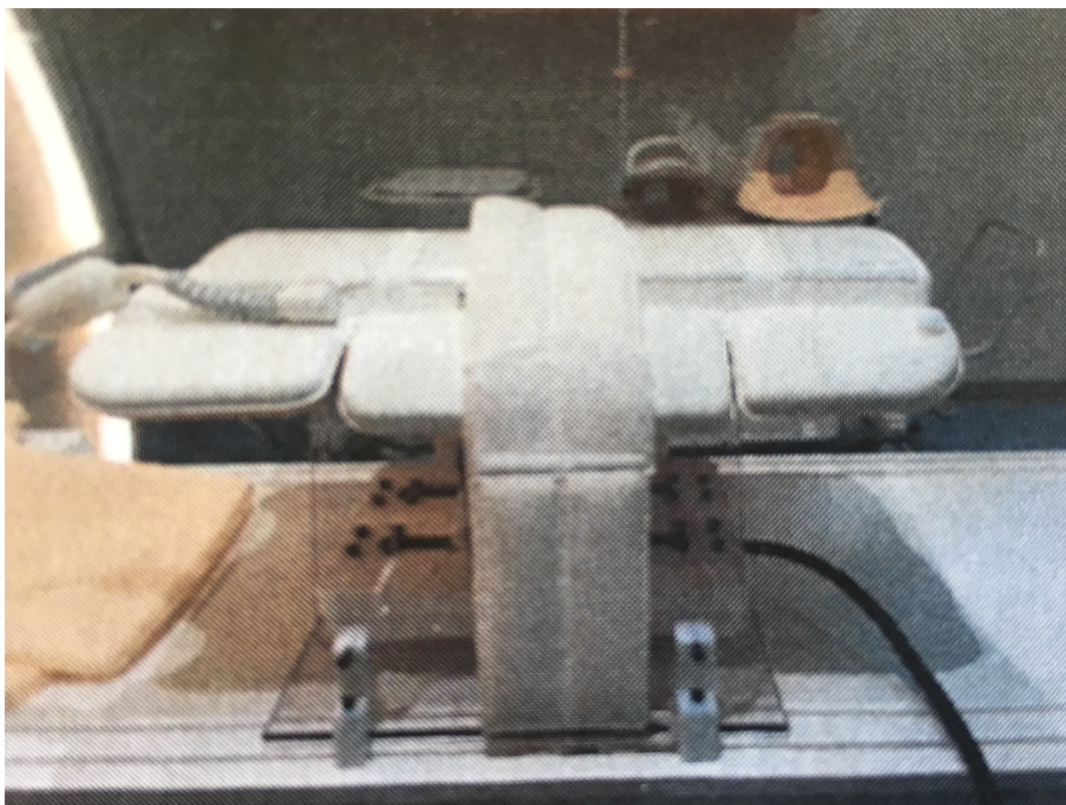


Figure 3.3. Motion platform with phantom and the body coil; the body coil includes 32 RF channels and sits on top of the phantom to provide a multichannel MR scan. The set up is ready for undergoing the data acquisition.

3.2 Motion Platform

An MRI-compatible motion platform is composed of two major parts: a controller that also contains the transporting cart, and a PC with a specifically designed interface (Labview) to communicate with the transporting cart. Signals from the PC are sent through two cables to the platform, and are translated to motion in the platform on the MRI table via two linear actuators. The PC remains in the control room while the transporter, including the motion platform, phantom and connector cables are placed inside the MRI room. The connecting cables pass through a filter

box in order to reduce the electrical interference that may cause MR image corruption.

On the MRI table, the platform is secured to the table using four side-in-soft-strap inserts that are used as mounting points for the plate holding the motion platform. The phantom is placed on the platform, and a known motion trace is programmed in the platform from the control room. The Labview program permits one dimensional trajectories between 1 cm to 12 cm. The motion trajectory can be from the embedded waveforms available on the motion platform, or programmed into the platform based on the interested properties of motion.

In this study, we focus on the motion of the abdomen due to the failure of the subject to hold his breath during a breath-hold scan. While breathing induced motion in the abdomen is complex, and consists of motion in all directions, we assume the motion to be in the longitudinal axis and to be linearly related to the motion of the chest or lungs in the transverse plane along the sagittal axis. This is a common assumption in Radiation Therapy, where breathing induced tumor motion has been found to be largest along the superior-inferior direction [46].

3.3 Programmed Motion Trajectories

Included with the motion platform are several examples of organ motion trajectories derived from motion tracking of MR images from patient scans [47]. We studied these sample traces to determine some of the characteristics of our motion trajectories. For instance, based on these traces, the amplitude of the motion is chosen to vary between 2-3 cm with the average duration of a breathing cycle assumed to vary from 3 to 6 seconds under normal respiration.

However, the motion traces supplied with the motion platform are complex as they include several factors such as noise, cycle to cycle variations, drift, etc. Since our goal is to investigate the impact of each one of these factors on the resulting artifacts, it is sensible to choose a set of trajectories with each trajectory focusing on only one aspect of the motion, i.e. a parametric study. For this reason, we focus on two types of motions present in patients: sudden motions would be caused by a patient's cough, and continuous drift motions as would arise from a patient who consistently maintains a low inhale or exhale over the duration of the breath-hold scan.

Several sinusoidal trajectories with variations in the period, amplitude and number of peaks were tested. Sudden motions can be modeled using a sinusoidal wave with a short period representing the short duration of the cough, and an amplitude representing the intensity of the cough. Drift type motions can be modeled using a sinusoidal wave with a large period, so that there is a monotone increase in the amplitude of the motion. Finally, simulating two or three sinusoidal peaks/coughs in a scan permits us to study the effect of short, periodic motion that is persistent throughout the scan.

For the sinusoidal trajectories used to simulate coughs, three factors were chosen to characterize the trajectory:

- Time of failure: the point in time that the subject coughs. This time defines the duration of the extent to which the K-Space was acquired prior to its corruption by the motion.
- Duration of motion: this quantity permits us to study the relation between the percentage of the K-Space that is corrupt with the type and intensity of the resulting artifact.

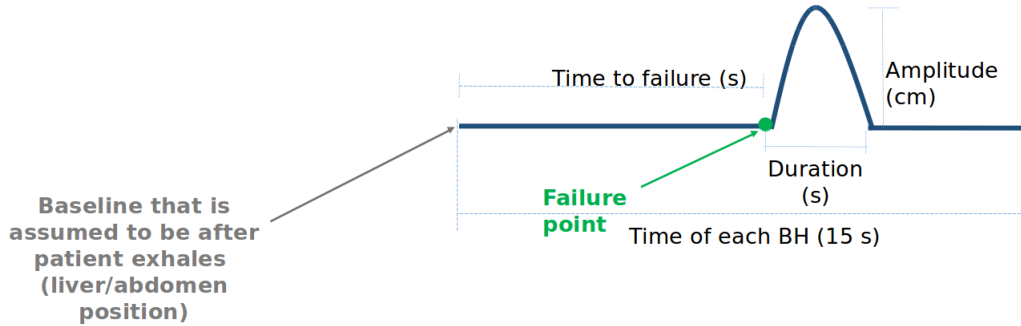


Figure 3.4. The general sinusoidal wave trajectory and its characteristic variables.

- Amplitude: this quantity is used to represent the depth of the motion (or breathing) and its effect on the artifact in the final image. It is shown in chapter 4 that, the larger the amplitude, the more intense the artifacts will be.

Drift type trajectories represent the patient's continuous inhale or exhale over the entire duration of the scan. As a result, the motion is not terminated at any point in the scan but rather represents a gradual rise or collapse of the lungs due to the patient's gradual but continuous inhale or exhale. Therefore, these trajectories are represented by a slowly varying sinusoidal wave with a long period. Two factors were chosen to characterize these trajectories:

- Time of failure: is again the moment that the patient starts to breath.
- Amplitude additionally represents the depth of breathing.

Figure 3.4 presents the parameters shown on a typical trajectory. The above parameters, along with their geometrical interpretation, are displayed in Figure 3.4. The horizontal blue solid line shows the baseline position of the phantom. The time to failure (in seconds) corresponds to the point in time where the motion occurs. The duration of the wave represents the breathing cycle length, and varies from 3 to 6 seconds. The amplitude of the trajectory represents the intensity of the motion, or the depth of breathing.

3.3.0.3 Trajectories for the first series of experiments

Parallel imaging with SENSE reconstruction was enabled in the first set of experiments. As a result, the duration of the scan time was 15 seconds. This is the minimum duration for which a trajectory must be defined; indeed, in order to avoid a sudden jump in the motion platform, the trajectories were defined for a period of 30 seconds (see next section).

By varying the parameters listed above, various trajectories are defined; for the first set of experiments, the results of the total number of five trajectories are presented in this report. Presented in figure 3.5 are trajectories representing short duration motion (such as coughs or hick-ups), and longer variations as would be caused by drifts (third row). As discussed in the previous section, a sinusoidal function is used to represent both types of motion, with drifts having a longer period.

Based on real patient data for liver motion, the trajectories were defined to have the following properties:

- Failure point: as the total scan time is 15 seconds, the chosen values correspond to the start, middle, and end of the scan time. The chosen values are:
 - after 1 sec,
 - after 7 sec,
 - at the end (12sec)
- Duration: this value represents how fast the individual manages to recover to breath-hold state, after failure. The chosen values are:
 - three seconds
 - six seconds
 - fifteen seconds

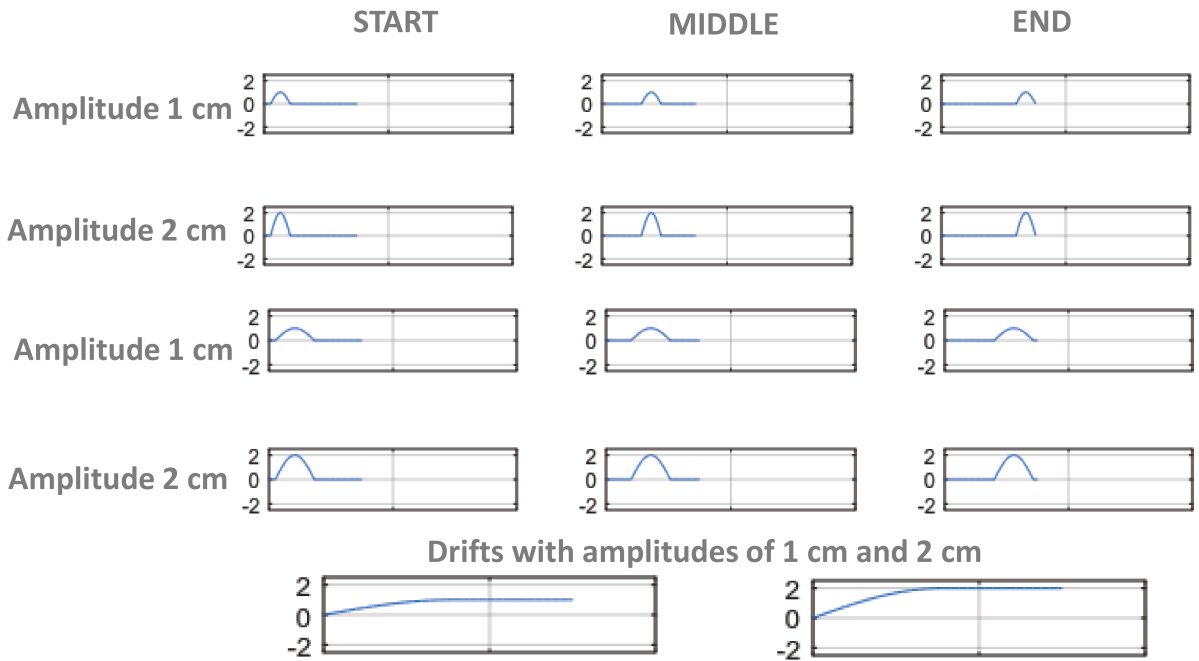


Figure 3.5. Attempted trajectories for the first set of experiments; first two rows are the trajectories that last for three seconds and occur at start (first column), in the middle (second column) and at the end (last column) of the data acquisition process; amplitudes are respectively 1 and 2 cm for the first and second rows. Third and fourth rows have the same order, while the duration of the motion is extended to 6 seconds. The last row presents drift failures with amplitude of 1 cm (left) and 2 cm (right).

- Amplitudes of 1 cm and 2 cm as reported in [47].

The above set of trajectories were programmed into the motion platform and scans were acquired according to the procedure outlined in section 3.1. The obtained experimental results (shown in chapter 4) were presented to an MD/physician who commented that usually, with healthy individuals, the failure of breath-hold occurs in the period between the middle to the end of the scan with the breathing cycle continuing after failure. Additionally, since the abdomen moves downward with exhale and returns to its upward positions at the start of inhale, it was suggested that the direction of motion be changed in-order to simplify visualization. These recommen-

dations were taken into account when contemplating the trajectories for the second experiment.

3.3.0.4 Second set of Experiments

The previous set of trajectories were constructed with the goal of classifying the resulting artifacts based on the motion type that they originated from. A second set of experiments were performed to investigate the possibility for correcting/reducing the impact of the artifact via manipulation of the K-Space. As the scanner reconstructed data only contains images, manipulating the K-Space requires access to the scanner raw data and reconstruction of the final image based on the corrected raw data. To simplify this process, parallel imaging is turned off, and SENSE reconstruction and aliasing corrections are not applied. As a result, the scan time increases and lasts approximately 35 seconds. Therefore, all trajectories for the second experiment were defined to last for at least 35 seconds.

The above trajectories were created to simulate:

- Breathing that begins at the start of the scan and continues through the entire length of the scan. The breathing cycle has a period of 3 seconds, which corresponds to the breathing cycle for a healthy individual.
- Breathing that begins at the middle of the scan and continues as normal through the entire length of the scan as a cycle with the period of 3 seconds.
- Breathing that starts at the end of the scan.
- A short duration, sudden motion at different times during the scan (start, middle and end). This represents a cough or short breath as it often occurs during breath-hold scans.

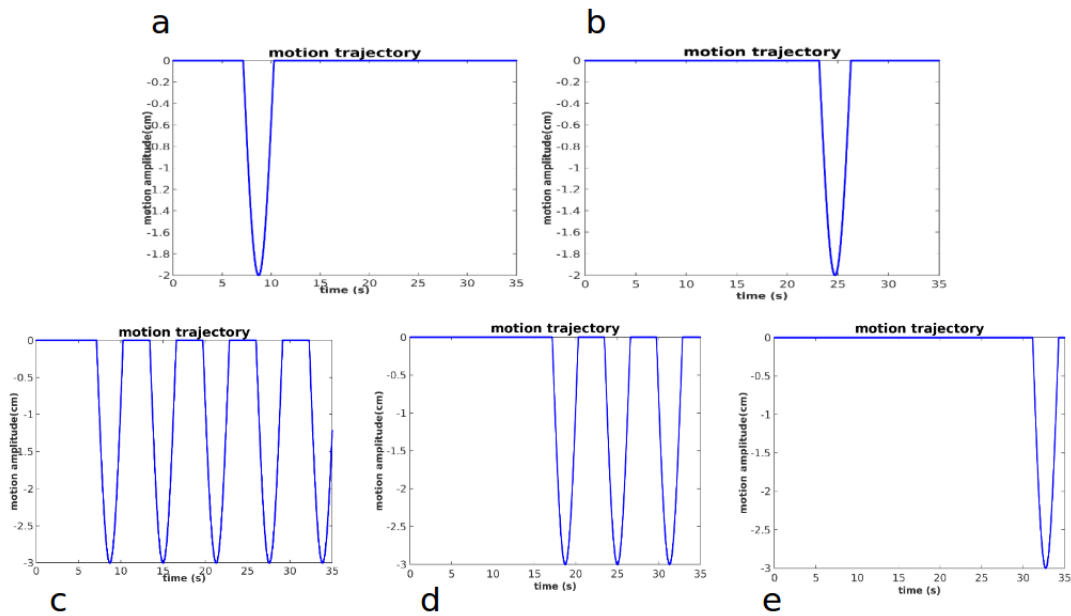


Figure 3.6. Trajectories for the second set of experiments; (a) and (b) are one sharp sinusoidal wave before (a) and after (b) the center of K-Space; the second row shows the trajectories with motion starting during the scan and continuing until the end. Panel (c) has the most corrupted data between, and (d) has the motion occur after the center of K-Space. Panel (e) has the least corrupted data and results in an image similar to the stationary scan.

Comparison of the first and second trajectories can highlight the effect that having a the motion prior or after the center of K-Space acquisition has on the final image. This information can provide some insight into the effect of the timing of the motion on the resulting image artifact (see chapter 4).

Figure 3.3.0.4 presents the motion trajectories. The first row presents the short duration, sudden motions that occur at the start of the scan (a), and later in the scan (b); the second row depicts the patient’s failure to hold his breath at the start (c), middle (d), and end of the scan (e).

3.4 MRI sequence

The MRI sequence must be chosen with the goals and characteristics of the study in mind. The MRI sequence used in this study is m-DIXON-W-BH-SENSE in the axial plane on an abdomen phantom. W in the name is related to m-DIXON method and stands for water since the method is known for separating fat and water. Axial plane refers to the imaginary horizontal plane that divides the body into superior and inferior parts; i.e. the SI plane, perpendicular to the coronal and sagittal planes. Selection of this plane permits a better visualization of organs such as liver, spleen, and kidneys as well as the spinal cord. Finally, BH refers to breath-hold scans, which is one of the most common strategies used to suppress respiratory motion artifacts in MR images and signifies the underlying issue that we are studying - motion correction.

The DIXON sequences in MRI are used to suppress fat in the image. Because of the abundance of fat in the liver (and also in our abdomen phantom), imaging the liver is one such case where fat needs to be suppressed. DIXON sequence [1] takes advantage of the difference in the frequencies of fat and water bound protons in MRI. The method acquires the signal twice: once at the center of the echo (when fat and water are in phase), and another with TE adjusted to the point where fat and water are out of phase. These two sets of images are added together (2.10) to create water only and fat only images according to the procedure outlined in section 2.2.

Table 3.1 reports the specifications of the used sequence. A repetition time of 3.355 milliseconds is chosen and the reconstructed field of view after zero filling/reconstruction is 400x229x400. We note that this is different from the raw data

size which is 171x121x71 points. The seemed increase in resolution is obtained by zero filling the K-Space (see below section on correction methods).

Parameters	m-DIXON-W-BH SENSE
Number of slices	131
Repetition time	3.355 milliseconds
FOV	400x229x400 voxels
Pixel Spacing	1x1x3.5 mm ³
Water fat shift	0.262 pixel
Scan mode	3D
Scan time	15.1 seconds
SliceThickness	3.5000 mm
Acceleration factor	1.5 in y direction / 0.5 in z-direction

Table 3.1. The sequence properties input for m-DIXON-W-BH SENSE. We note that the scan mode we have used is in 3D and spans 131 slices permitting for a FOV of 400x229x229 voxels after zero filling.

Figure 3.4 presents a K-Space trajectory obtained from the second set of experiments. The presented K-Space trajectory is a partial acquisition in Z (second phase encoding direction) by 15%, i.e. 15% of the K-Space (in k_z direction) is not acquired. Figure (a) shows the order that k_y points are acquired with respect to the scanner time. The total scanner time is 35 seconds, so that in all three graphs, the x-axis represents the interval $[0, 35s]$, i.e. the 10682 points. This number represents the total number of points acquired by the scanner over this time interval. The interval between each pair of k_y points is the TR: in this time interval, all the k_x and k_z points related to the specific k_y are acquired. Figure 3.4 (b) shows the trajectory that the K-Space is acquired; for each k_y point in figure (a) there is a line of k_z points acquired. Its important to note that not all k_z lines have the same number of data points, i.e. not all k_z points are acquired for each k_y . Indeed the oval shape of the

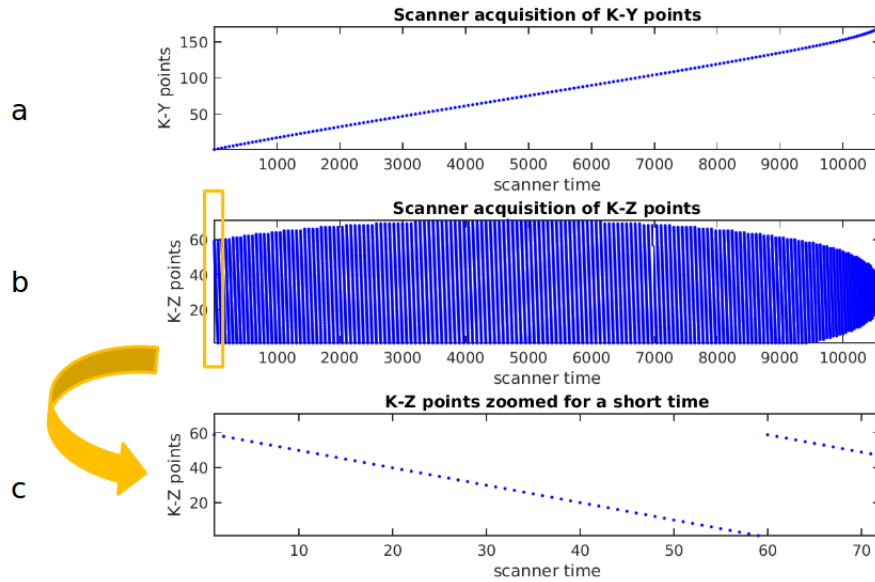


Figure 3.7. Indices for K-y and K-z acquisition; (a) shows K_y points being acquired as a function of the scan time, (b) represents how K_z are acquired from minimum number 1 k_z point to maximum number of 71 k_z points. Not all K_z points are acquired for every K_y and this makes processing more difficult; K_x plane is composed of 456 points, acquired simultaneously meaning that for every single point in K_z graph (b) there are 456 points in frequency encoding direction that are filled almost at the same time, (c) Depicts one of the lines of K_z from (b) to make it easier to understand the way each k_z line is acquired.

acquired K-Space highlights the fact that the number of data points collected in the k_z direction decreases near the edges of the graph. Although figure (b) is plotted using solid blue points as markers, the high density of the total number of points in the scan time (10682 points in 35 seconds) makes distinguishing between the different k_y points difficult. Figure (c) shows a zoomed-in version of one of the lines in the second graph and presents how the k_z are being acquired with time. Per each point in the second diagram, 171 k_x points are acquired in the read-out direction perpendicular to the $k_y - k_z$ plane. In comparison to the phase encoding directions (k_y and k_z), the acquisition process in this direction can be assumed as simultaneous.

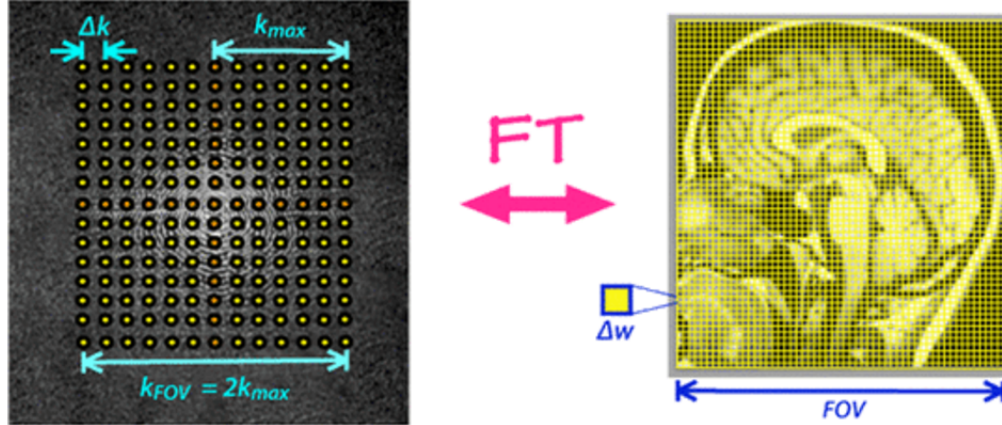


Figure 3.8. Reproduced from '<http://mriquestions.com/field-of-view-fov.html>'; The distance between two entries of a 2D K-Space (here Δk) is inversely related to the extent of FOV and pixel size (Δw) and from symmetry considerations an inverse relation exist between $k_{FOV}(= 2K_{x,max})$ and spatial resolution (pixel size) in image domain (Δw). The K-Space, and image are assumed to be quadrangular meaning $FOV_x = FOV_y = FOV$ and $\Delta x = \Delta y = \Delta w$.

3.5 K-Space Manipulation

Since the K-Space and the final MR image are directly related, properties of the K-Space correspond to properties in the image. For example, the resolution in the image domain is related to the interval distance between two consecutive data points in the K-Space. If the Field-of-view (FOV) is the length of MR image in each direction (in mm or cm), then the units establishing the 2D FOV are pixels, with the pixel size determining the resolution of the image. In figure 3.5, the pixel size is represented as Δw . This pixel size and accordingly FOV are inversely proportional to the number of data points in K-Space in each direction; this relations is presented in equations 3.1 and 3.2:

$$\Delta w = \frac{1}{k_{FOV}} \quad (3.1)$$

$$\Delta k = \frac{1}{FOV} \quad (3.2)$$

Observed from the above equations is that the extent/width of the FOV is inversely proportional to the interval size of the frequency domain. Conversely, the width of the K-Space is inversely related to the pixel size or spatial resolution of the image. In most correction algorithms, this relation results in a constraint regarding how much of the image can be recovered from an incomplete K-Space acquisition.

Many algorithms attempt to use the K-Space as a source of additional information or a data base that can be reversely manipulated to enhance the quality of the reconstructed image. The K-Space can even be used to estimate the motion in the subject, and attempt to correct for the detected motion without using navigator or gated breathing apparatus [48].

3.6 Methods for K-Space Correction

Faster MR imaging is a common desire amongst clinicians and researchers. One of the ways to reduce scan times is via partial data acquisition methods coupled with various reconstruction techniques [5]. In this study, we investigate the possibility of applying some of such methods to correct for motion artifacts.

The strategies that we investigate involve removal (and perhaps correction) of the corrupted sections of the K-Space, and reconstruction of the images from the corrected K-Space. Many classical algorithms exist for this purpose such as: Zero Padding (or filling), Phase Correction using conjugate symmetry, and Homodyne

reconstruction [49]. In chapter 4, we present some of our results using zero padding to correct for the motion.

3.6.1 Correction via zero padding

Motion artifacts arise from the acquisition of the incorrect position in the object. The inconsistent/corrupted K-Space can lead to the effects outlined in section 2.6. When the corrupted sections of the K-Space are set to zero, errors arising from motion will not be present. Of course, this is not expected to completely resolve artifacts (a portion of the K-Space has not been acquired). However, this precise reasoning lies behind many partial acquisition correction techniques - if the acquired portion of the K-Space is greater than 8/9, then the reconstructed image can be expected to be of good quality.

3.6.2 Correction via the conjugate symmetry rule

When the nature of the acquired image permits, the missing points of the K-Space may be estimated using the conjugate symmetry rule with symmetric lines passing through the center of the K-Space used to remove the phase error. Let $M_s(k_x, k_y)$ be a symmetric central region of the K-Space and $I_s(x, y)$ be its reconstructed image. The correction method consists of three steps:

1. the image $I_s(x, y)$ is multiplied by a phase correction multiplier $p^*(x, y)$ to produce a phase corrected image $I_{pk}(x, y)$. The Fourier transform of this image will result in the phase corrected K-Space.
2. the phase corrected K-Space can now be completed using the conjugate symmetry rule.
3. the phase corrected completed K-Space can now be used to generate the corrected image.

The phase correction multiplier $p^*(x, y)$ is defined as [49]:

$$p^* = e^{-i\phi^*}(x, y) \quad (3.3)$$

where $\phi^*(x, y)$ is the argument of the image (phase) (usually the argument of $M_s(k_x, k_y)$ is used instead).

The main draw back of using the conjugate symmetry is the assumption that the entries of K-Space are imaginary. As a result, in cases where the K-Space is real, or close to being real, this approach will not yield much improvement.

3.7 Data Analysis

The goal of this work and the experiments performed in its frame-work is to investigate the possibility of manipulating the K-Space to reduce motion artifacts. To do this, we generated a set of libraries in matlab that permit for the manipulation of the scanner obtained raw data and implementation of various correction techniques. Thus-far zero padding has been applied with promising results presented in chapter 4.

Manipulation of the K-Space requires access to the scanner acquired raw data. Each scan has two files associated with it whose extensions are '.dat' and '.list'. The '.list' file contains information pertinent to the encoding of the '.dat' file. Our code first reads the K-Space from these files and manipulates it according to the following algorithm:

1. the information from multiple coils are combined to generate a guess image for the static scan.
2. channel error weighting factors ϵ_{ic} are computed and a final static image is generated using the error weighting factors.

3. raw data '.list' and '.dat' files are read and the K-Space data $K(k_x, k_y, k_z, ic, ie)$ is loaded into memory for each of the coils ic and echoes ie .
4. trajectories $f_y(t)$ and $f_z(y(t), t)$ are constructed by sorting the '.list' information and the K-Space trajectory is generated (see figure 3.4).
5. the motion trace/programmed trajectory $s(t)$ is used to generate the multiplier $\lambda(t)$ varying between 0 and 1; $\lambda = 1$ when the object is static (no motion), and $\lambda = 0$ when the object is in motion. A moving-window filter is applied to smooth the variation between 0 and 1 to reduce ringing artifacts in the final image.
6. for time t , the partially acquired K-Space $K_{ic}(t)(k_x, k_y, k_z, IE)$ is obtained by multiplying the raw data with the multiplier $\lambda(t)$. $K_{ic}(t)$ represents the portion of the K-Space acquired by the scanner at time t . Multiplication by $\lambda(t)$ ensures that the portions of the K-Space obtained during motion are neglected.

$$K_{ic}(t)(k_x, k_y, k_z, ie) = \lambda(t) \cdot K(k_x, k_y(t), k_z(y(t), t), ic, ie) \quad (3.4)$$

7. an image is produced for each channel by taking the Inverse Fourier transform of its K-Space. Images from the multiple coils are combined using the error factors ϵ_{ic} (from step 2) to generate a final image.

Last two steps in the above algorithm are performed for each $t = T_y$ corresponding to the start of a new y point acquisition. An animation of the K-Space is obtained exhibiting the growth of the K-Space as a function of time. Studying this K-Space permits for a deeper understanding of how the image is influenced by the points in the K-Space.

Care must be exercised when combining the information acquired by each coil. The number of coils displayed in the raw data varies from scan to scan, and depends

on the quality of the image and is chosen by the scanner. Each coil creates an image that has higher signal intensities near its location. Combination of the coils by simply using their geometric average may not lead to an ideal image. This is presented by the top image in figure 3.7, which shows poor comparison with the scanner reconstructed DICOM (bottom image).

In-order to produce a more acceptable image, we combine the coils by weighting them with an error weighting factor ϵ_{ic} . For a static image (no motion during acquisition), we combine coil information in a two step procedure to compute the final image; first a guess image IMG^1 is obtained by simply averaging over the coils, so that:

$$\text{Guess image } IMG^1 = \frac{1}{N_{channels}} \sqrt{\sum_{ic=1}^{N_{channels}} IMG_{ic} \cdot \bar{IMG}_{ic}} \quad (3.5)$$

Next, for each channel/coil, an error weighting factor ϵ_{ic} is computed as the difference between the coil image IMG_{ic} and the guess image IMG^1 :

$$\text{error for each coil } \epsilon_{ic} = IMG_{ic} - IMG^1 \quad (3.6)$$

The errors are then normalized such that the sum of their squares adds to unity $\sum_{ic=1}^{N_c} \epsilon_{ic}^2 = 1$. The final image IMG^2 is then obtained by combining the information for each channel using the weighting factor $\frac{1}{\epsilon_{ic}}$.

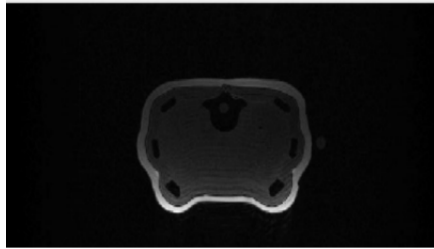
$$\text{final image } IMG^2 = \sqrt{\sum_{ic=1}^{N_{channels}} \frac{1}{\epsilon_{ic}^2} (IMG_{ic} \cdot \bar{IMG}_{ic})} \quad (3.7)$$

The result is an improvement in the final image, observed in the second pannel in figure 3.7.

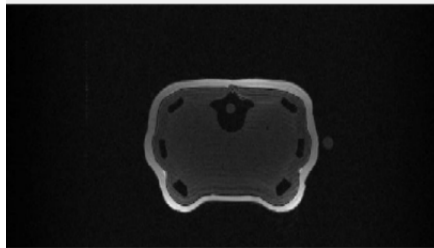
Figure 3.10 presents a flow chart of the methodology used in this work to perform and analyze the experiments. Motion trajectories are constructed and MRI

scans are performed using the mDixon sequence. Scanner reconstructed DICOMs are used as a validation, while scanner raw data is extracted and processed using our MATLAB libraries according to the algorithm described above. When $t = t_f$ is the final time of the scanner, the obtained image is motion corrected using zero-padding algorithm.

Simple averaging over coils



Using error weighting



Scanner DICOM

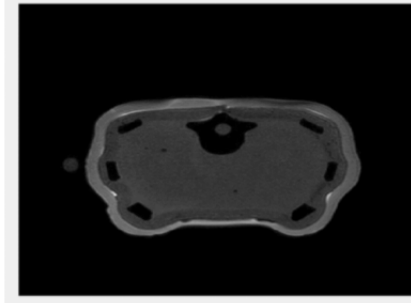


Figure 3.9. Coil averaged image vs. scanner reconstructed DICOM: simple averaging over coils does not lead to a reasonable image (first row); a guess image is defined and weighting factors are assigned to each coil defined using the error of the coil image and the guess image. Channels with a lower error are given a higher weighting. The image at the bottom is the scanner reconstructed image to be compared with the result of our simplified version.

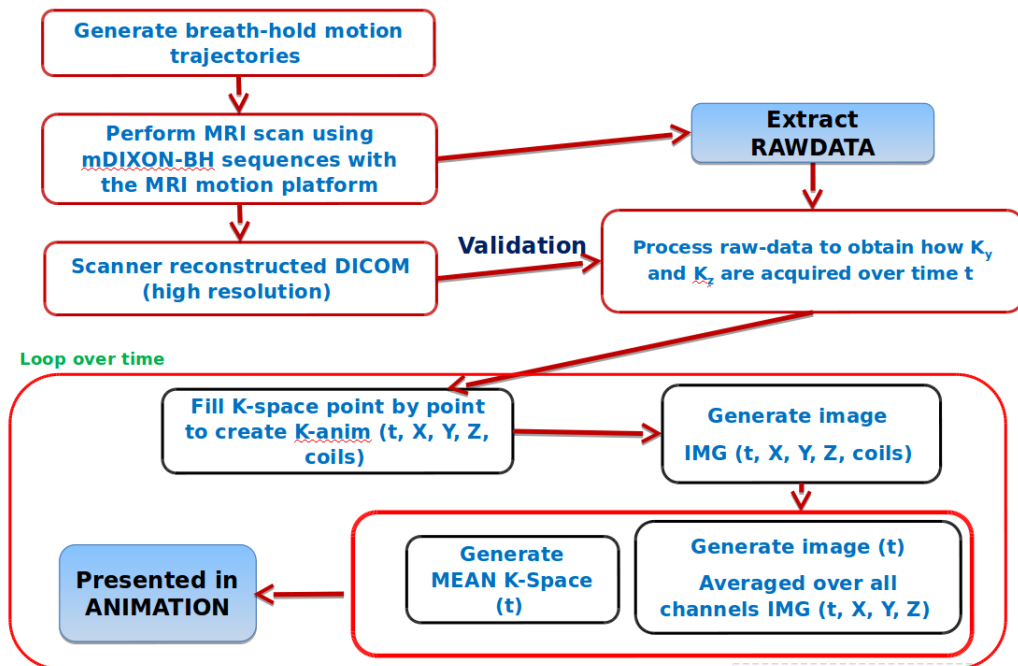


Figure 3.10. Flow chart for processing and correcting the raw data.

CHAPTER 4

Results

This chapter presents our results and analysis for two sets of experiments performed over the course of this study; the first examines the resulting type of artifacts in terms of their underlying trajectories with the aim of investigating the type of artifacts that are most common to breath-hold exams. After consulting with a trained physician, we performed a second set of experiments with new trajectories chosen to investigate the potential possibility of correcting for respiratory motion artifacts using data processing methods.

4.1 First Set of Experiments

In this set of experiments, we perform a parametric study of motion artifacts with respect to the base parameters that characterize their motion trajectory. According to the methodology presented in section 3.3.0.3, variation of the artifact is studied with respect to: the starting time of the occurrence of motion, the duration of the motion, and its amplitude. Each one of these parameters impacts the corruption of the K-Space and hence the final image.

The impact of the above parameters can be measured by where and how they affect the K-Space with respect to the center of K-space acquisition. While all points in the K-Space contribute to the image, the importance of each point in the K-Space can be weighed by the contribution of its amplitude in the Fourier series representation of the final image. As points with lower frequencies tend to have the largest

contributions, a good knowledge of their values is essential to the image. This can be observed from figure 4.1 which presents the contribution of the central portion or the outer portion of the K-Space to the final image. The top row corresponds to an image reconstructed after removing the central portion of the K-Space. What is observed is a heavily degraded final image (second column), highlighting the importance of the lower frequency data points found near the center of the K-Space. The second row presents the image reconstructed after removing the periphery of the K-Space. Although approximately $2/3$ of the K-Space has been removed in this second case, we observe a significantly sharper image than the previous, indicating the lower importance of points located at the periphery.

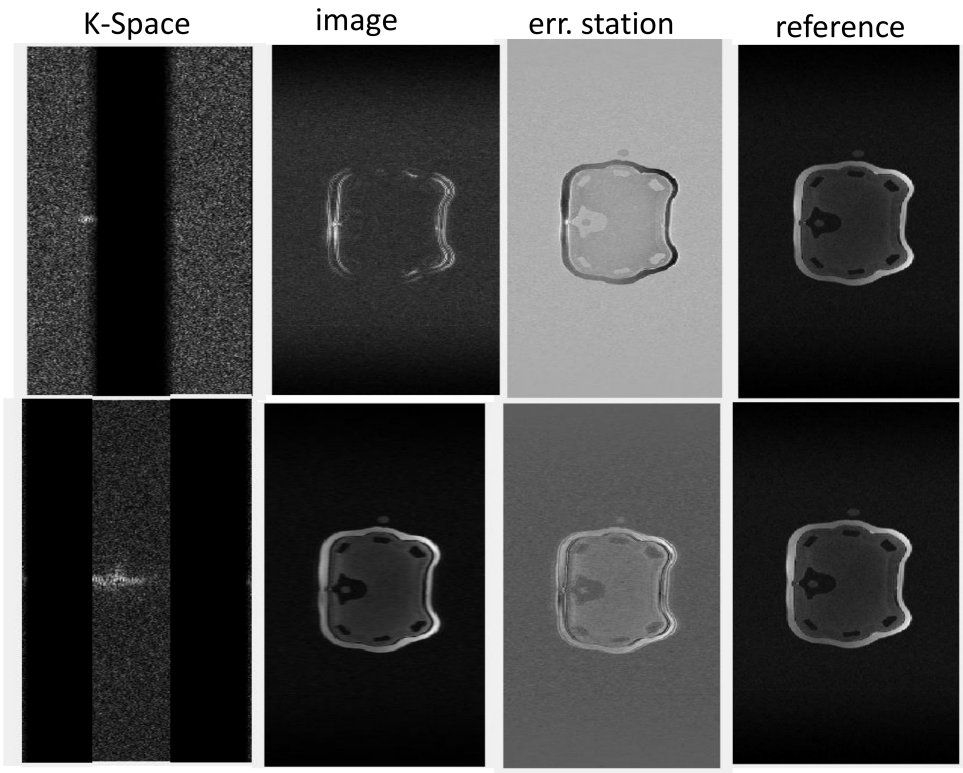


Figure 4.1. Contribution of the central and periphery of the K-Space to the final image. Presented in each row are the K-Space, the corresponding image, its error with the reference/stationary image, and the reference image. The top row corresponds to the image obtained after the removal of the center of K-Space and the bottom row corresponds to the image obtained after removal of the periphery of the K-Space.

Variation of the artifact with respect to the starting time is dependent on the specific region of the K-Space that is being acquired. This can be observed from the different columns in figure 4.2; the first row in the figure represents the artifact ridden image. The second row represents the error due to motion and is calculated as the difference between the obtained image and the artifact-free reference/static image. The last row depicts the motion trajectory that was programmed into the motion platform. We observe from the figure that the greatest degradation is seen for the trajectory depicted in the first column: since the duration of the scan is short (15 s), the programmed motion coincides with the acquisition of points near the center of K-Space. As these points represent information corresponding to lower frequency entries in the Fourier series, knowledge of their correct values is necessary for an accurate representation of the object. The second and third columns correspond to the motion occurring at a time where points further away from the center of K-Space are being acquired, i.e. during the acquisition of higher frequencies components. As we will see in the next figure, a good knowledge of such information permits for an accurate representation of small objects, sharp edges and those requiring high resolution.

Results: effect of time of failure

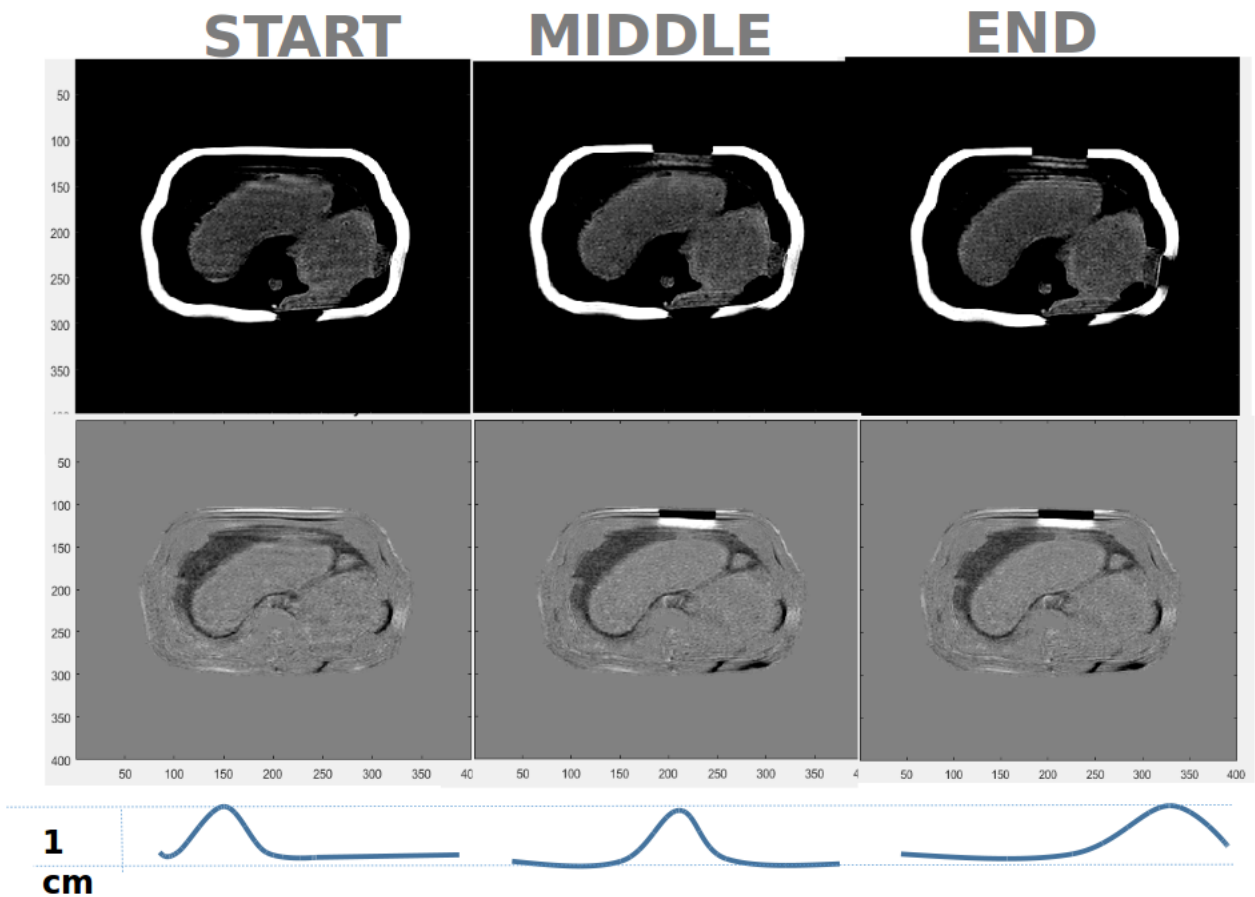


Figure 4.2. Comparison of the motion artifacts due to motion occurring at the start, middle and end of the scan. The first column presents the final image (first row) and the associated error due to occurrence of motion at the start of the scan. The column presents the final image and its associated error due to the motion occurring at the middle of the scan, and the last column corresponds to the final image and its associated error due to motion occurring at the end of the scan.

Figure 4.3 presents the impact that varying the duration of motion has on the resulting artifact. Observed in the figure is the inter-play of two effects: starting time and velocity of the motion. Firstly, a degradation in image A (similar to the previous image) is observed corresponding to a 3 seconds trajectory occurring at the start of the scan. As discussed above, the degradation is due to the lack in low frequency amplitudes. The middle column presents an even further degradation in the image (a higher intensity of artifacts is present), particularly at the edges of the image which require accurate knowledge of higher order frequencies. This occurs because the longer duration of motion (6 seconds) results in a larger corruption of the K-Space, while the intensity (velocity) results in bulk motion effects. The third column in the figure corresponds to a motion occurring over the entire duration of the scan. However, the velocity of the motion is low (duration is twice as long as previous column), so that the phantom movement is too slow to have a great effect on the final image. Here, what is observed is a systematic loss in signal intensity, represented by the inverted image observed in the error.

Results: effect of failure duration

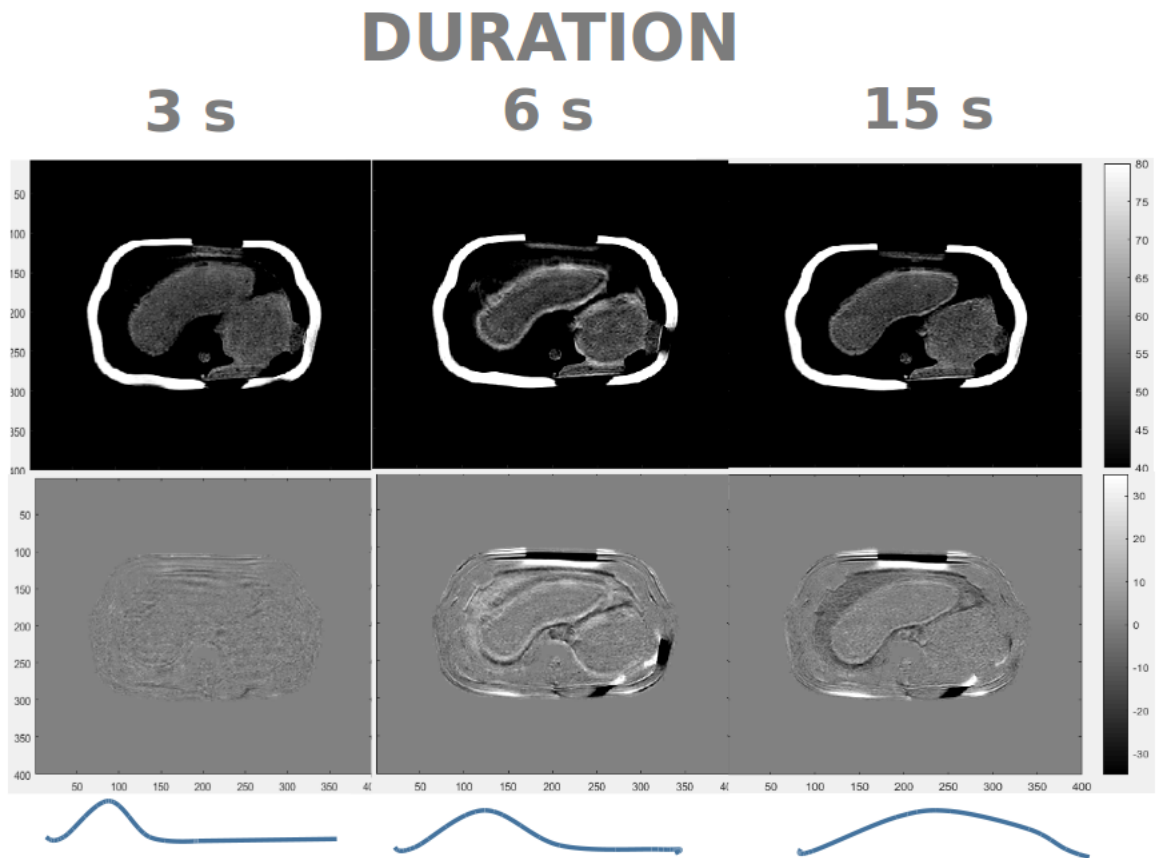


Figure 4.3. Impact of the duration of motion on the motion artifact. The first column represents the final image (first row) and its error with the stationary (second row) due to a 3 seconds trajectory occurring at the start of the scan. The second column presents the final image and its error occurring at the middle of the scan. The last column presents the final image and its error due to a motion consistent over the entire duration of the scan.

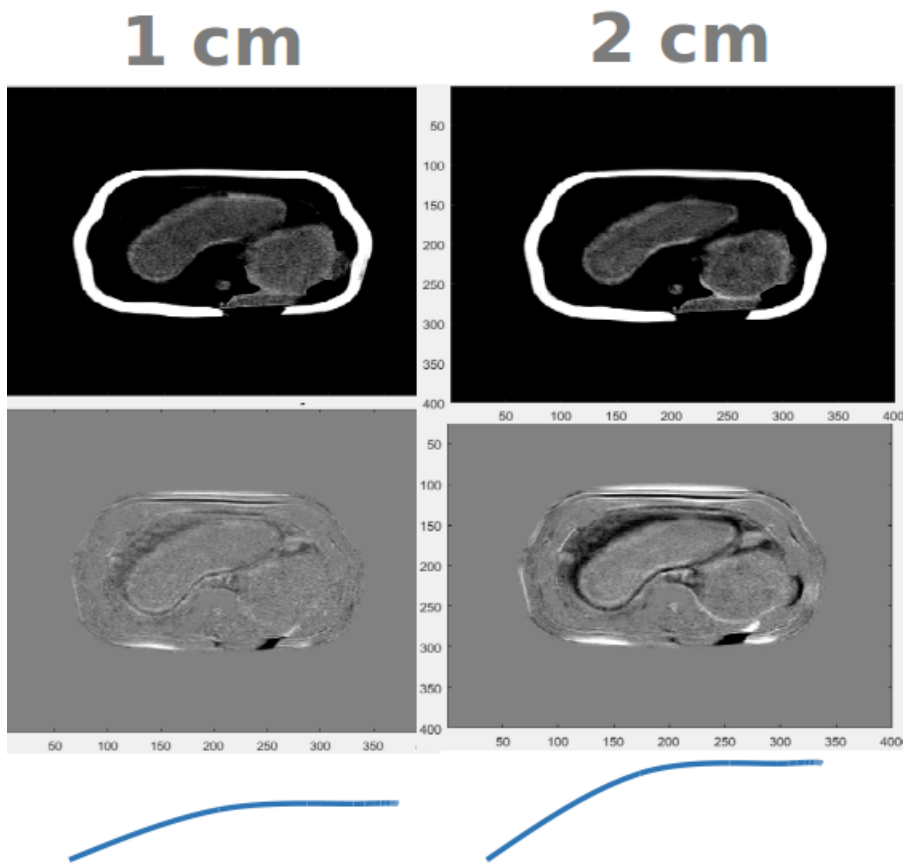


Figure 4.4. Comparison of motion artifacts for drifts of 1 cm and 2 cm respectively. Presented in the first column are the final image and the error for a 1 cm drift. The second column presents the final image and its error for a 2 cm drift.

Figure 4.4 presents drifts with amplitude of 1 and 2 centimeters in first and second columns respectively; result is an increase in the intensity of artifact from the amplitude of the drift.

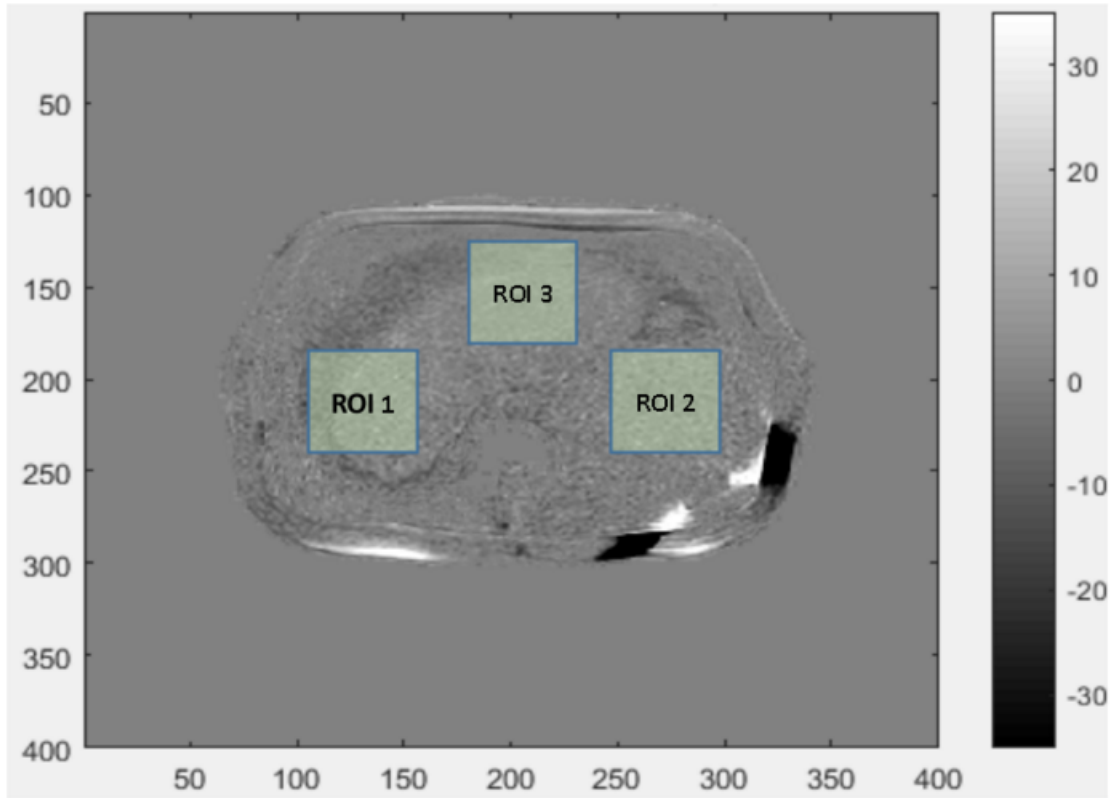


Figure 4.5. Regions of interest in the phantom. ROI 1 contains homogeneous tissue for two organs, including their boundary. ROI 2 contains homogeneous tissue representing a single organ. ROI 3 is composed of fat with the largest level of ringing observed in the previous figures.

Figure 4.5 exhibits three regions of interest (ROI) that are chosen to calculate the root mean square. The three ROIs include properties of the figure such as:

- ROI 1 contains homogeneous tissue for two organs, including edges.
- ROI 2 contains homogeneous tissue representing a single organ.
- ROI 3 is composed of fat with the greatest ringing observed in the above figures.

From the above experimental results and their analysis we observed that:

- the intensity of the artifact increases with increasing amplitude so that a deeper breath would result in a worsening of the artifact.

Table 4.1. RMSE of the object image with respect to the reference stationary. ϵ_{SS} represents the background noise and is computed as the RMSE of two measurements of the stationary phantom. $\epsilon_{A,T}$ represents the RMSE of the image obtained from motion of amplitude A (in cm) at time T (in s). ϵ_A represents the drift of intensity A occurring at time T . The RMSE has been calculated according to $RMSE = \frac{1}{m \cdot n} \sqrt{\sum_{i=1}^{M-1} \sum_{j=1}^{N-1} [I_{ij} - I_{s,(i,j)}^2]^2}$ with M, N are the number of pixels in the X and Y direction respectively, and $I_{s,(i,j)}$ representing the stationary reference image.

	ϵ_{SS}	$\epsilon_{2cm,T=0s}$	$\epsilon_{2cm,T=7s}$	$\epsilon_{2cm,T=12s}$	$\epsilon_{1cm,T=0s}$	$\epsilon_{1cm,T=7s}$	$\epsilon_{1cm,T=12s}$	ϵ_{1cm}	ϵ_{2cm}
1	3.98	3.30	15.18	3.07	5.52	5.40	3.36	4.86	11.46
2	3.07	3.27	9.20	3.10	4.77	5.52	3.27	3.48	4.06
3	2.72	4.69	27.03	3.04	4.99	5.20	3.22	3.15	4.54

- a quicker/higher velocity motion results in higher intensities of the artifact.
- worse artifacts occur when the motion overlaps with the center of K-Space acquisition.

We presented and discussed our results with a trained physician/MD in the UTSW radiation oncology department who confirmed that the artifacts observed in the above figures mimic those encountered in daily clinical practice. Based on his suggestions, a second set of experimental studies were designed to investigate the possibility for motion correction using K-Space manipulation.

4.2 Second Set of Experiments

In this second set of experiments, raw-data is extracted from scanner and directly analyzed; the raw data contains the acquired K-Space for each of the N_{COILS} coils, and includes the K-Space trajectory that were used to acquire the points. To inspect visually the acquisition of the K-Space, an animation is generated from the raw data that portrays the evolution of the image with acquisition. The repercussions of the motion on the K-Space and the reconstructed image are then be studied from this animation. Using the input trajectory programmed into the motion platform as a navigator, we isolate the region of K-Space that was acquired at the time of motion. To correct for the motion, we define a multiplier $\lambda(t)$ that equals to unity when the object is stationary and zero when the object is in motion. Multiplying the K-Space points by this multiplier results in a K-Space that with values obtained during the occurrence of motion suppressed. Figure 3.10 in chapter 3 presents the methodology for the analysis of our results.

4.2.1 Motion before and after the center of K-Space acquisition

Figure 4.6 presents the final images and their K-Spaces obtained after the occurrence of the trajectory profile (red curve) during the scan. The two trajectories presented here are similar in both amplitude and duration. The only variable has been the starting time. Since the Cartesian K-Space is symmetric (see section 2.3), we could expect the two resulting images to be similar since they approximately occur at the same time interval from the middle of the scan. However, as observed from the figure, the artifacts observed in the two images are quite different; the reasoning for this could be due to the unsymmetrical nature of the K-Space trajectory that was presented in figure 3.4, which results in an unequal number of data points on each side of the K-Space center.

Figure 4.7 presents the multiplier (in red) used for compensating for the motion, as well as the motion corrupted K-Spaces corresponding to the previous figure. A filtering is applied to the step function to avoid sharp cuts in the K-Space (this leads to ringing artifacts). The multiplier takes zero values for non-zero trajectory. Multiplying the K-Space by this multiplier results in discard of points during the occurrence of motion. The corrected K-Spaces are presented in the second column of the figure, with the error presented in the third column. Observed from the figure is the reason for the difference between the two images in figure 4.6: for motion occurring in the first row, a portion of the center of K-Space is obtained during the motion. In the second row, these lower frequencies are completely acquired prior to the motion. As a result, the intensity of the artifact is greater for the first case.

By zero-padding the K-Space according to the previous figure, we can hope to improve/alleviate the artifact. Figure 4.6 presents the corrected image for each of the

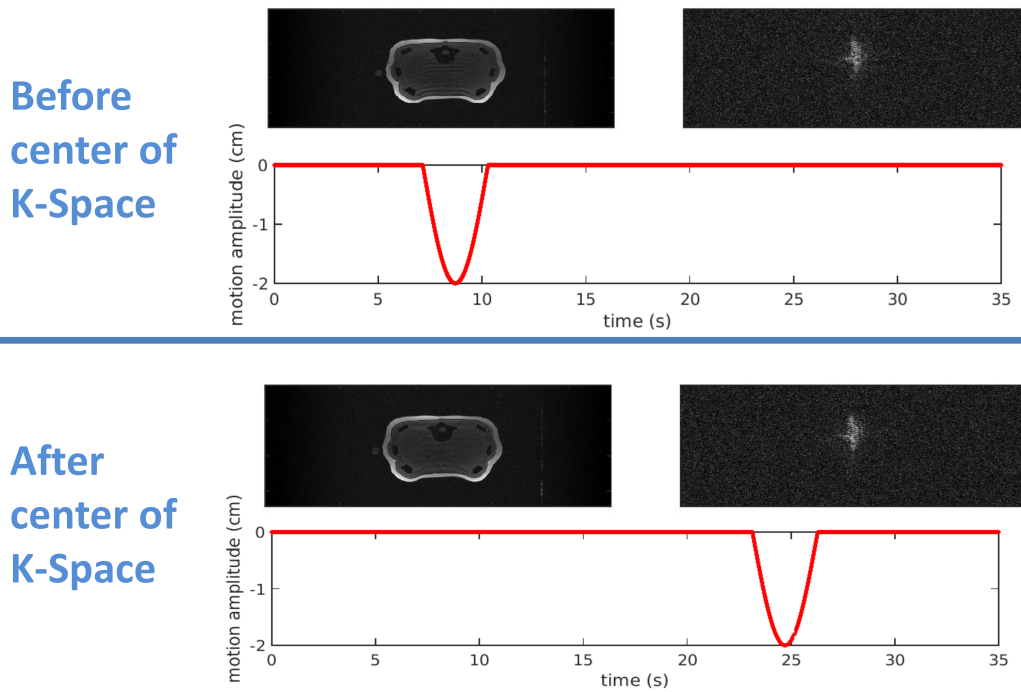
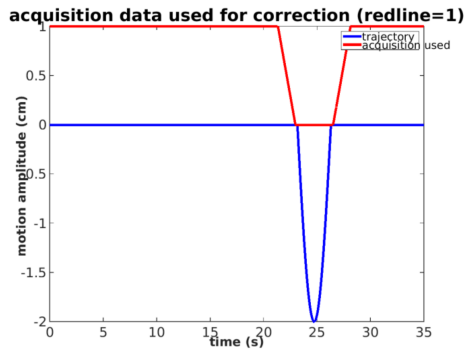
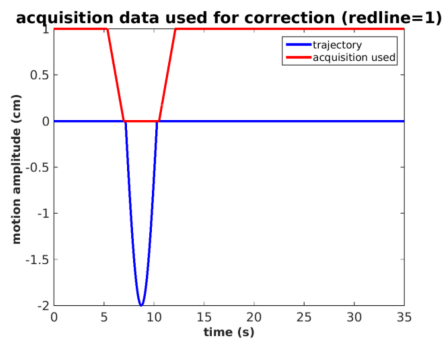


Figure 4.6. Comparison of motion artifacts for motion occurring before and after the middle of the scan time. Top row presents the image and the corresponding K-Space obtained from the motion trajectory (red) occurring prior to the middle of the scan. The bottom row presents the image and its corresponding K-Space as obtained from the motion trajectory after the middle of the scan.

two trajectories. Since points from the center of K-Space are discarded in the first trajectory, zero-padding does not lead to a noticeable improvement of the results. However, zero-padding leads to an improvement in the second trajectory, where we observe the error image to mimic the actual image (i.e. the result is a reduction in the ringing artifact at the cost of a loss in signal intensity).

Trajectory



K-Space

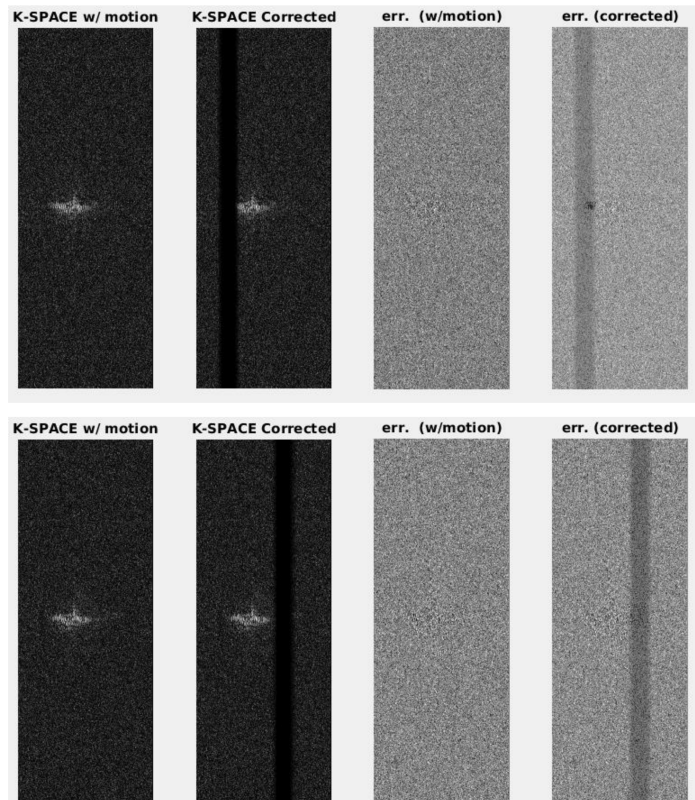


Figure 4.7. Correction multiplier and the corrected K-Spaces. Presented in the figure are the K-Space corrupted by motion, the zero-padded K-Space and their respective errors with the K-Space of the stationary image.

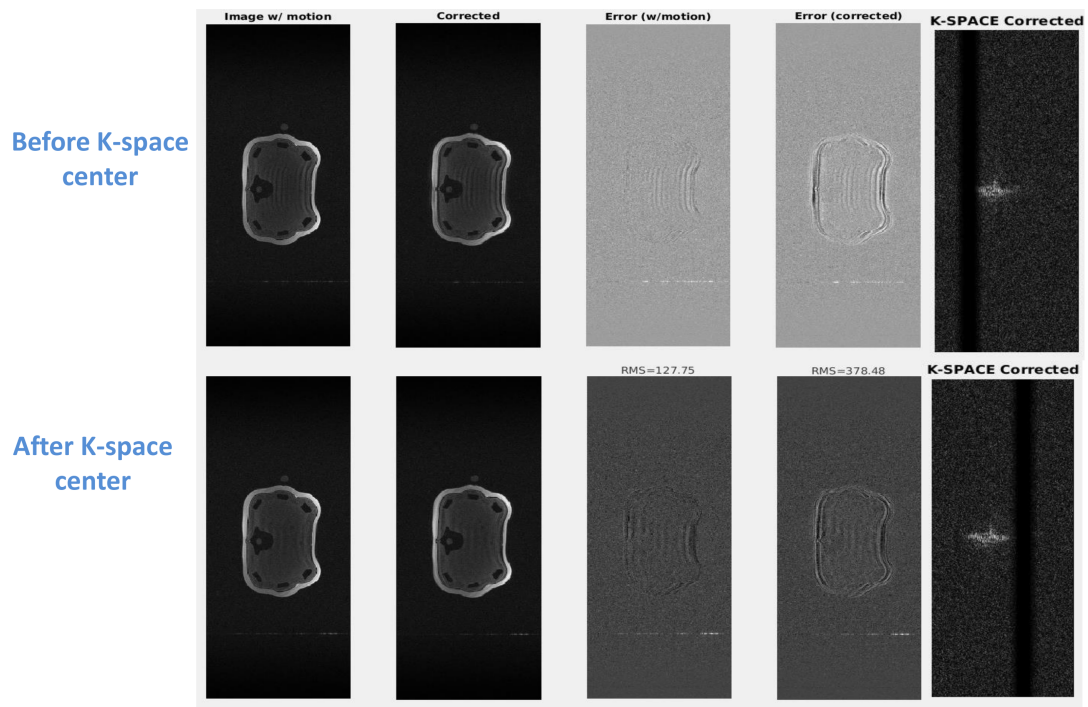


Figure 4.8. Comparison of the image prior to zero padding and after zero padding. Top row presents images corresponding to motion occurring prior to the center of the scan. Bottom row presents Reconstructed images after the center of the scan. Presented in each row are the artifact ridden image, the corrected/zero padded image, and their respective errors with the stationary profile as well as the corrected K-Space.

4.2.2 Motion occurring during the scan and continuing to the end

This second set of trajectories simulate breath-hold failures that continue to occur until the end of the scan. The result for three such trajectories are presented in figures 4.2.2, 4.10, and 4.11 with the duration of the trajectory decreasing for each consecutive figure. The artifact ridden image and its K-Space are presented in the first column, with results obtained from zero-padding presented in the second column.

Comparison of the final image for each of the three trajectories shows that decreasing the extent of the corrupted region of the K-Space results in an improvement in the obtained image (lower intensity of artifacts). Additionally, a smaller corrupted region also permits for correction using zero-padding; this can be observed in figures 4.10, and 4.11 where zero-padding is seen to lead to an improvement. In the case where at least half of the K-Space has been obtained, zero-padding seems to yield an improvement in the results. This can be observed in figure 4.10, where the ringing artifacts have been removed by zero-padding at the cost of a higher SNR.

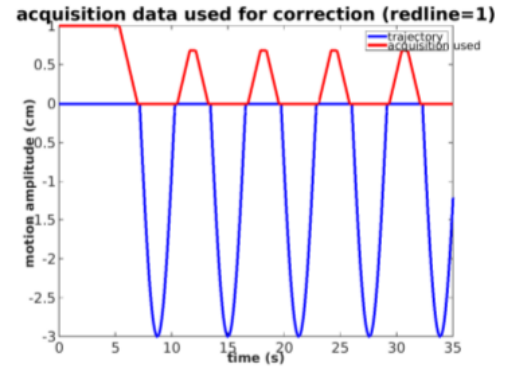
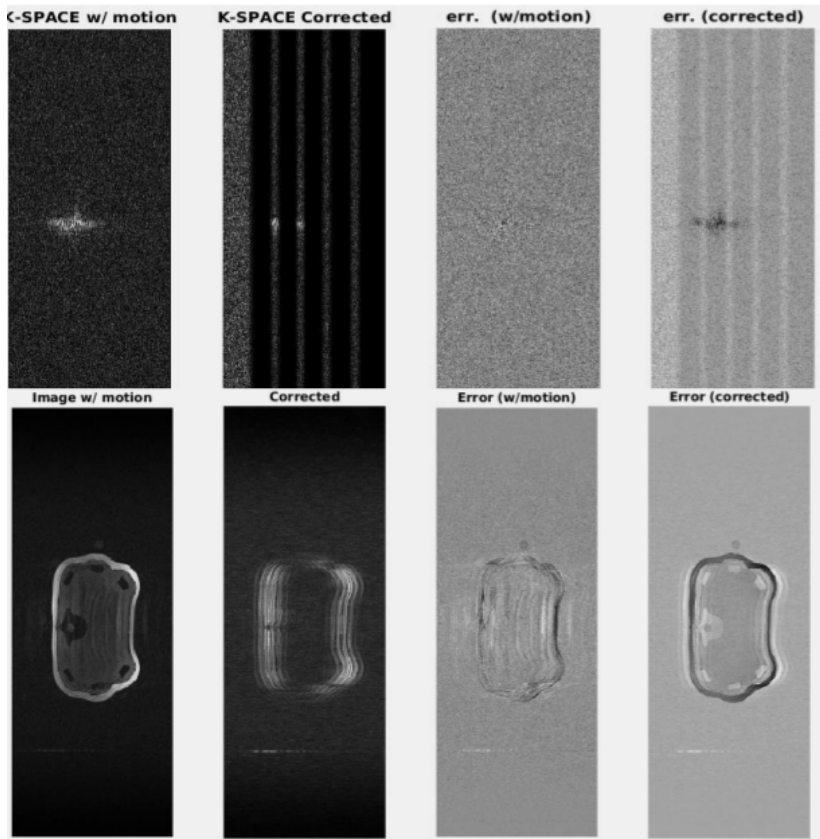


Figure 4.9. K-Space and final image for motion that occurs near the start of the scan and continues well until the end. The first row presents the corrupted K-Space, the zero padded K-Space and their errors with respect to the stationary reference. The second row presents images corresponding to the K-Spaces presented in the first row.

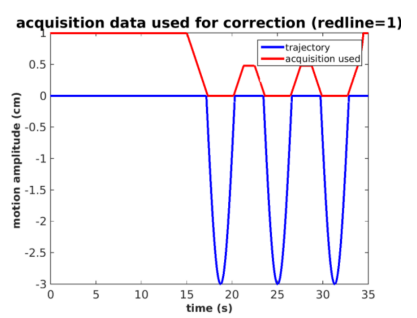
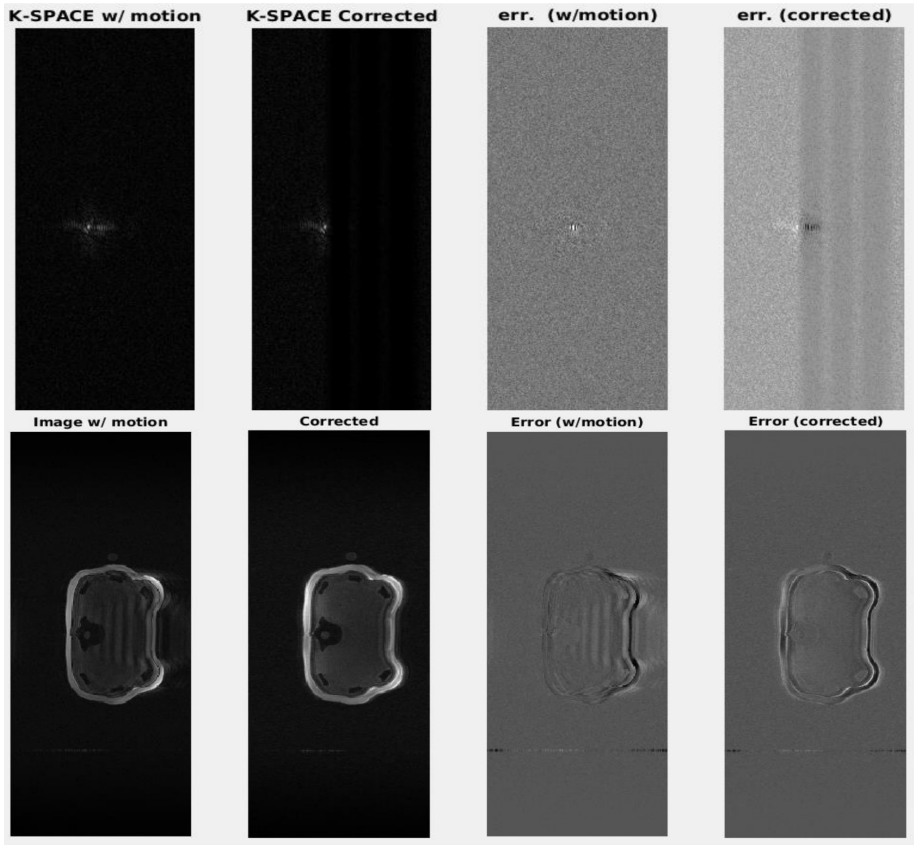


Figure 4.10. K-Space and final image for motion that occurs at the middle of the the scan and continues well until the end. The first row presents the corrupted K-Space, the zero padded K-Space and their errors with respect to the stationary reference. The second row presents images corresponding to the K-Spaces presented in the first row.

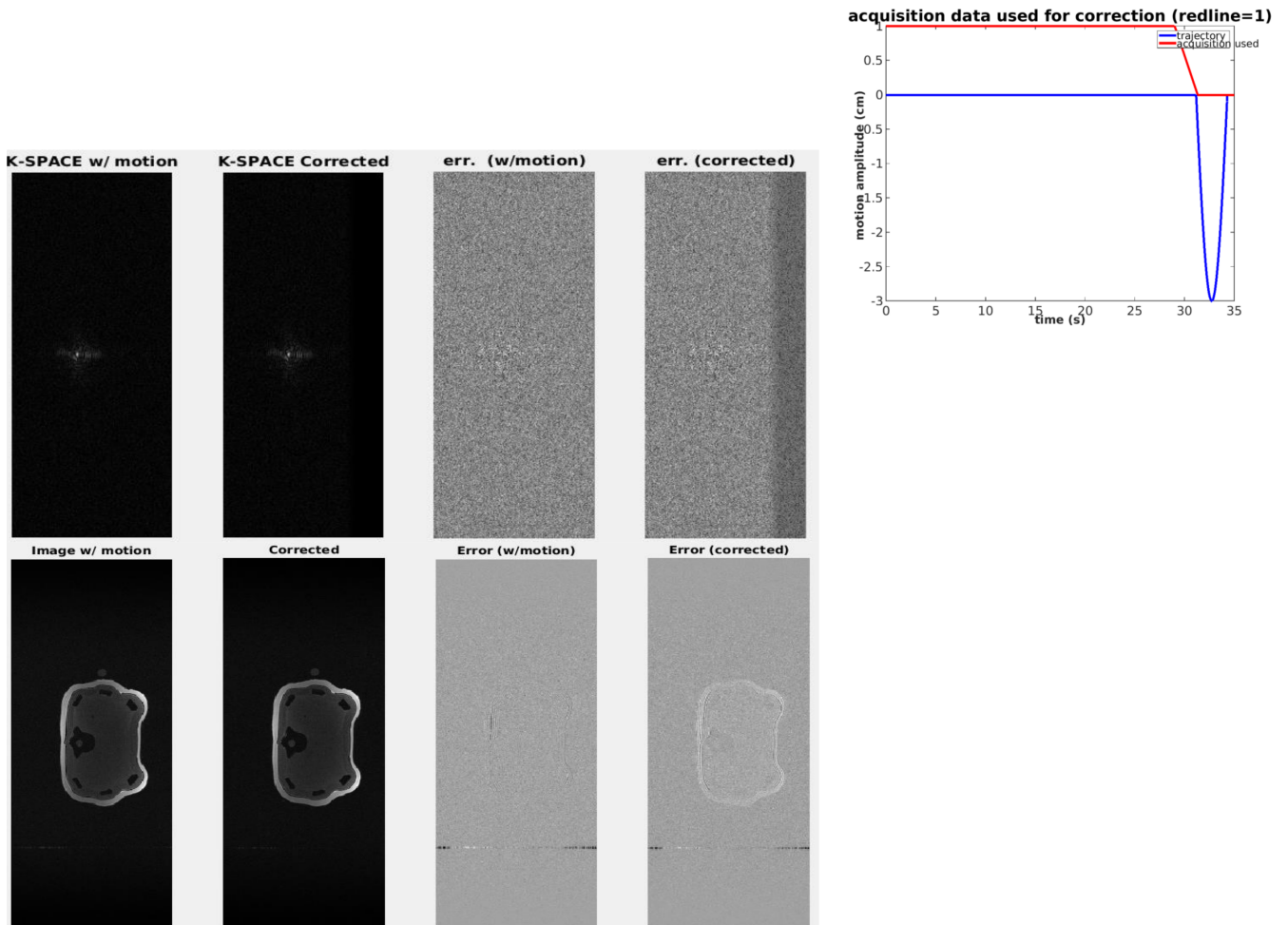


Figure 4.11. K-Space and final image for motion that occurs near the end of the scan and continues well until the end. The first row presents the corrupted K-Space, the zero padded K-Space and their errors with respect to the stationary reference. The second row presents images corresponding to the K-Spaces presented in the first row.

CHAPTER 5

Concluding Remarks

The occurrence of motion during the data acquisition process is not only a major problem in MRI but for all imaging modalities. The change in patient's anatomy is often unaccounted for during the image generation resulting in the wrong registration of the location of the subject, thereby leading to an un-real image containing motion artifacts. Such motion artifacts, whose properties are dependent on the characteristics of the underlying motion, can hinder accurate diagnosis thereby reducing the clinical value of the image. While many methods have been devised to address this issue, a simple to implement and yet clinically translatable approach is yet to be proposed.

This study investigated the potential applicability of K-Space manipulation methods for motion artifact correction in breath-hold MR scans of the abdomen. To do this, an MRI compatible motion platform, mounted with an abdomen phantom was used to simulate the motion artifacts that are most common to breath-hold scans. By representing the motion in terms of sinusoidal waves, a parametric study was performed relating the artifact to underlying characteristics of the motion such as: the timing of the failure in holding the breath, the amplitude of the motion and the duration of the motion. Data from several hours of measurements at the RTR MR scanner (UTSW) was then processed to study the variation of the motion artifact with each of these parameters. Additionally, a set of tools in MATLAB was developed for the analysis, manipulation, reconstruction and possible correction of the artifact using

the scanner generated raw data (K-Space).

Our experimental analysis showed that the intensity of the artifact tends to increase with the magnitude and velocity of motion. Additionally, the time of the occurrence of motion was found to have a great impact on the intensity of the artifact; our results presented in chapter 4 highlighted the importance of the K-Space center and demonstrated that when the occurrence of motion overlaps with the center of K-Space acquisition, the corruption in the low frequency data leads to a much higher intensity artifact than as would occur for motion else-where during the acquisition process. While application of our tools to correct for motion using zero-padding cannot compensate for such a scenarios, it showed promising results for cases where the center of K-space was already acquired. Indeed, for cases where the motion occurred after the middle of the scan, zero padding reduced the intensity of the artifact at the cost of a higher SNR.

While zero-padding provides a simple way to compensate for the corrupted K-Space, it does not utilize all the properties and information available from an MR scan. Application of partial acquisition methods to motion correction may provide a more flexible strategy for this cause. Conjugate symmetry, homodyne reconstruction and parallel imaging methods such as GAPPA reconstruction are partial acquisition strategies that take advantage of additional properties of the K-Space to compensate for missing information. Such algorithms have the potential to be implemented using our tools and may provide an improvement in our results.

For example, by taking advantage of the conjugate symmetric nature of the K-Space, more accurate values can be substituted for the corrupted ones. However, a

possible disadvantage of this approach is the assumption that entries in the K-Space are imaginary. As a result, in cases where the K-Space is real, or close to real, such an assumption will not yield improvements. Homodyne reconstruction techniques use the same conjugate property of the K-Space but reduce the number of Fourier transforms that are required, thereby decreasing the numerical complexity, and noise hence speeding up the reconstruction process.

Finally, the GRAPPA reconstruction method is a promising parallel imaging method that aims to provide an accurate estimation using coil sensitivity maps. The corrupted points can be recalculated using a kernel that extracts phase information from the symmetrically acquired portions of the K-Space. Implementation and application of GRAPPA using our tools may provide a precise and robust strategy for motion correction using K-Space manipulation.

APPENDIX A

MATLAB code for Raw Data Analysis tool

A.0.3 Main code

```
1 clear all;
2 close all;
3 src='./09122015MR.mat/' ; %source for the processed matfiles
4 images='./images/' ; %location to write images to
5 traj_src='./09122015MRI/' ; %locations where trajectories are stored
6 mfile_src='./mfiles/' ; %location to store matlab files (NOT USED).
7
8 series={'13', '14', '15', '16', '17', '18', '21', '32'} %SERIES TO BE ANALYZED
9 IZ_SLICE=70; %SLICE TO BE ANALYZED
10 z_lo=41; z_hi=106; %%Z-SLICES TO BE USED IN IMAGE WEIGHTING
11 dT_mri=20.e-3; %TIME STEP OF THE MRI MOTION PLATFORM
12 t_f=35.0; %FINAL SIMLUATION/TRAJECTOR TIME
13 T_err=1.0; %error between trajectory and mri motion
14 stationary='raw_005_rawdata.mat';
15
16
17 %%%
18 %%LOAD STATIONARY DATA
19 %CREATE RAW IMAGE, MEAN IMAGE, AND K_MEAN FOR STATIONARY
20 %%%
21 station=load(sprintf('%s%s', src, stationary));
22 station.out_dir=images;
23 station.name='stationary' ;
24 station.z_lo=z_lo; station.z_hi=z_hi;
25 station.sqzrawdata=squeeze(station.rawdata);
26 [station.IX, station.IY, station.IZ, station.IE, station.IC]
27 =size(squeeze(station.rawdata));
28 [S2.IMG_RAW, S2.IMG_MEAN, S2.K_MEAN]=create_avg_img(squeeze(station.rawdata), station.ky,
29 station.kz);
30 [station.IMG_MEAN, station.K_MEAN, station.err, station.IMG_RAW]
31 =create_avg_img_err(squeeze(station.rawdata), station.ky,
32 station.kz, station.z_lo, station.z_hi, S2.IMG_MEAN, 0, 0);
33 sprintf('\nSTATIONARY READ\n')
34
35
36 %%%%%%%%%%%%%%%%%%%%%%%%%%%%%%%%%%%%%%%%%%%%%%%%%%%%%%%%%%%%%%%%%%%%%%%%%
37 %%%%%%%%%%%%%%%%%%%%%%%%%%%%%%%%%%%%%%%%%%%%%%%%%%%%%%%%%%%%%%%%%%%%%%%%%LOOP OVER SERIES
38 %%%%%%%%%%%%%%%%%%%%%%%%%%%%%%%%%%%%%%%%%%%%%%%%%%%%%%%%%%%%%%%%%%%%%%%%%
39 for dummy=1:length(series)
40 close all;
41 series_num=series{dummy}; %SERIES NUMBER
42 sprintf('\n\n PROCESSING SERIES %s', series_num)
43
44
45 traj_file=sprintf('series_%s.txt', series_num);
46 avi_name=sprintf('raw_%s', series_num);
47 mfile_name=sprintf('%s%s.mat', mfile_src, avi_name);
48
49
50 traj_path=sprintf('%s%s', traj_src, traj_file);
```



```

51 %LOAD STATIC DATA
52 %%%%
53 static1=load(sprintf('%sraw_0%s_rawdata.mat', src, series_num));
54 static1.name=sprintf('raw_0%s', series_num);
55 static1.out_dir=images;
56 %%%%
57 %CREATE RAW IMAGE, MEAN IMAGE, AND K_MEAN FOR STATIC PROFILES
58 %%%%
59 %ind_ic=[3:1:10 16:20 22 23];
60 static1.sqzrawdata=squeeze(static1.rawdata);
61 [static1.IX, static1.IY, static1.IZ, static1.IE, static1.IC]=size(squeeze(static1.rawdata));
62
63 %%%%
64 %GENERATE A GUESS AVERAGE IMAGE
65 %%%%
66 [S1.IMG_RAW, S1.IMG_MEAN, S1.K_MEAN]=create_avg_img(squeeze(static1.rawdata), static1.ky,
67 static1.kz);
68 %%
69 %%APPLY WEIGHTING BY CHANNELS
70 %%
71 static1.z_lo=z_lo; static1.z_hi=z_hi; %%Z-SLICES TO BE USED IN IMAGE WEIGHTING
72
73 %%%%
74 %CALCULATE ERROR (OUTPUT IN static.err) AND CREATE AVERAGE IMAGE WITH CHANNELS
75 % WEIGHTED AS 1/ERR^2
76 [static1.IMG_MEAN, static1.K_MEAN, static1.err, static1.IMG_RAW]=
77 create_avg_img_err(squeeze(static1.rawdata),
78 static1.ky, static1.kz, static1.z_lo, static1.z_hi, S1.IMG_MEAN, 0, 0);
79 %%
80
81
82 %%%%
83 %FIND INDICES FOR KY AND SORT ACCORDINGLY
84 %%%%
85 IC=static1.IC;
86 [static1.f_y, static1.ind_hi_y, static1.ind_low_y, static1.dT_y, static1.T_acq_y]=
87 find_index_y(static1.ky(IC+1:end), static1.IC, static1.IE);
88 %%%%
89 %FIND INDICES FOR KZ AND SORT ACCORDINGLY
90 %%%%
91 [static1.f_z,static1.ind_hi_z, static1.ind_low_z, static1.dT_z, static1.T_acq_z, static1.TIME]=
92 find_index_z(static1.kz(IC+1:end), static1.IC, static1.IE);
93
94
95 %%%%%%%%%
96 %%BEGIN TO FILL K-SPACE POINT BY POINT, ADVANCING AT EVERY TSTEP
97 %%%%%%%%%
98 TSTEP=22000; %STEP SIZE TO BE USED IN THE ANIMATION
99 [static1.K_anim, static1.kxy_p, static1.IMG_anim, static1.IMG_anim_mean,
100 static1.K_anim_mean, static1.K_chan1, static1.times]=animation(static1, IZ_SLICE, TSTEP)
101 static1.DELTA_X=0.1*static1.IX;

```

```

102     static1.DELTA_Y=0.3*static1.IY;
103     %% READ AN INTERPOLATE TRAJECTORIES
104     %%%
105     [static1.traj_int, static1.time_int]=traject(traj_path, t_f, dT_mri, static1.times{end}(1));
106     %%FOR STATIC FILE ONLY
107
108     avi_path=sprintf('%s%s/', images, avi_name);
109     try
110         avi_path=sprintf('%s%s/', images, avi_name);
111         mkdir(avi_path);
112     catch
113         avi_path=sprintf('%s%s/', images, avi_name);
114     end
115     avi_file=sprintf('%s%s_%d.avi', avi_path, avi_name, IZ_SLICE);
116     static1.avi_path=avi_path;
117
118     try
119         make_movie(static1, static1.K_chan1, squeeze(static1.IMG_anim_mean(:, :, :, 1)),
120                 static1.kxy_p, static1.times, avi_file, IZ_SLICE)
121     catch
122         failed=1;
123     end
124
125     %%%
126     %%CORRECT FOR MOTION
127     %%%
128
129     %CONSTRUCT MARGIN CORRECTED TRAJECTORY
130     [static1.ind_corr, static1.ind]=add_margin_traj(T_err, static1.time_int, static1.traj_int)
131     static1.ind_corr=smooth(double(static1.ind_corr), 1.5e3, 'moving');
132     TSTEP=22000
133     [static1.K_anim_corr, static1.kxy_p_corr, static1.IMG_anim_corr, static1.IMG_anim_mean_corr,
134         static1.K_anim_mean_corr, static1.K_chan1_corr, static1.times_corr]=
135         corr_animation(static1, IZ_SLICE, TSTEP)
136
137     %%%%%%%%%%%%%%%%%%%%%%%%%%%%%%%%%%%%%%%%%%%%%%%%%%%%%%%%%%%%%%%%%%%%%%%%%
138     %%%%%%%%%%%%%%%%%%%%%%%%%%%%%%%%%%%%%%%%%%%%%%%%%%%%%%%%%%%%%%%%%%%%%%%%%PPPPLLLLLLOOOOOOOOTTTTTSSSSSSSS%%
139     %%%%%%%%%%%%%%%%%%%%%%%%%%%%%%%%%%%%%%%%%%%%%%%%%%%%%%%%%%%%%%%%%%%%%%%%%
140     %%%%%%%%%%%%%%%%%%%%%%%%%%%%%%%%%%%%%%%%%%%%%%%%%%%%%%%%%%%%%%%%%%%%%%%%%
141     %%% TRAJECTORIES
142     %%%%%%%%%%%%%%%%%%%%%%%%%%%%%%%%%%%%%%%%%%%%%%%%%%%%%%%%%%%%%%%%%%%%%%%%%
143     figure();
144     plot(static1.time_int, static1.traj_int, 'b.');
```

```

153
154     %%%%%%%%%%%%%%%%%%%%%%%%%%%%%%%%%%%%%%%%%
155     %%%TRAJECTORY WITH CORRECTION
156     %%%%%%%%%%%%%%%%%%%%%%%%%%%%%%%%%%%%%%%%%
157     figure();
158     tmp=static1.ind_corr ;
159     plot(static1.time_int, static1.traj_int, 'b', 'LineWidth', 3); hold();
160     plot(static1.time_int, tmp, 'r', 'LineWidth', 3);
161     xlabel('time (s)', 'FontWeight', 'bold', 'FontSize',15); ylabel('motion amplitude (cm) ',
162           'FontWeight', 'bold', 'FontSize', 15); title('motion trajectory');
163     xt = get(gca, 'XTick'); set(gca, 'FontSize', 16);
164
165     pngname=sprintf('%s%s.png', avi_path, 'trajectory_w_acq');
166     legend({'trajectory', 'acquisition used'}, 'FontSize', 13);
167     title('acquisition data used for correction (redline=1)', 'FontSize', 20);
168     set(gcf, 'units', 'normalized', 'outerposition', [0 0 1 1]);
169     print(pngname, '-dpng');
170
171     %%%%%%%%%%%%%%%%%%%%%%%%%%%%%%%%%%%%%%%%%
172     %%%%%%%%%          F_Y AND F_Z
173     %%%%%%%%%%%%%%%%%%%%%%%%%%%%%%%%%%%%%%%%%
174     figure();
175     subplot(3, 1, 1); plot(static1.f_y(:, 1), static1.f_y(:, 2), 'b. ');
176           xlabel('scanner time'); ylabel('K-Y points');
177     xlim([min(static1.f_y(:, 1)), max(static1.f_y(:, 1))]); ylim([min(static1.f_y(:, 2)),
178           max(static1.f_y(:, 2))]); title('Scanner acquisition of K-Y points');
179
180     subplot(3, 1, 2); plot(static1.f_z, 'b. '); xlabel('scanner time'); ylabel('K-Z points');
181     xlim([min(static1.f_y(:, 1)), max(static1.f_y(:, 1))]); ylim([min(static1.f_z),
182           max(static1.f_z)]); title('Scanner acquisition of K-Z points');
183
184     subplot(3, 1, 3); plot(static1.f_z, 'b. '); xlabel('scanner time'); ylabel('K-Z points');
185     xlim([min(static1.f_y(:, 1)), min(static1.f_y(:, 1))+max(static1.f_z)]);
186           ylim([min(static1.f_z), max(static1.f_z)]);
187     set(gcf, 'units', 'normalized', 'outerposition', [0 0 1 1]); title('K-Z points zoomed for a
188           short time')
189
190     pngname=sprintf('%s%s.png', avi_path, 'f_xy');
191     print(pngname, '-dpng');
192     %%%%%%%%%%%%%%%%%%%%%%%%%%%%%%%%%%%%%%%%%
193     %%%COMPARISON OF FIGURES AT THE END OF THE SCAN TIME USING THE AVERAGING
194     %%%%%%%%%%%%%%%%%%%%%%%%%%%%%%%%%%%%%%%%%
195     %%%%%%%%%%%%%%%%%%%%%%%%%%%%%%%%%%%%%%%%%
196     %%%%%%%%%%%%%%%%%%%%%%%%%%%%%%%%%%%%%%%%%
197
198     figure();
199     tmp1=S1.IMG_MEAN(:, :, IZ_SLICE, 1); tmp1=abs(tmp1)/sum(sum(abs(tmp1)));
200     tmp2=static1.IMG_MEAN(:, :, IZ_SLICE, 1); tmp2=abs(tmp2)/sum(sum(abs(tmp2)));
201     subplot(1, 3, 1); imagesc(tmp1); colormap gray; axis off; title('averaged w/ channels',
202           'FontSize', 12); axis off;
203

```

```

204 subplot(1, 3, 2); imagesc(tmp2); colormap gray; title('averaged w/channels w/ error
205         weighting', 'FontSize', 12); axis off;
206
207 subplot(1, 3, 3); imagesc(tmp2-tmp1); colormap gray; title('absolute difference',
208         'FontSize', 12); axis off;
209
210 set(gcf, 'units', 'normalized', 'outerposition', [0 0 1 1]);
211
212 pngname=sprintf('%s%s', avi_path, 'comparison_of_averaging');
213 img=getframe(gcf);
214 imwrite(img.cdata, [pngname, '.png']);
215
216
217 %%%%%%%%%%%%%%%%%%%%%%%%%%%%%%%%%%%%%%%%%%%%%%%%%%%%%%%%%%%%%%%%%%%%%%%%%%%%%%%COMPARISON FOR MOTION CORRECTION
218 %%%%%%%%%%%%%%%%%%%%%%%%%%%%%%%%%%%%%%%%%%%%%%%%%%%%%%%%%%%%%%%%%%%%%%%%%%%%%%%
219 %COMPARISON OF IMAGES
220 %%%%%%%%%%%%%%%%%%%%%%%%%%%%%%%%%%%%%%%%%%%%%%%%%%%%%%%%%%%%%%%%%%%%%%%%%%%%%%%
221 figure();
222 reference=station.IMG_MEAN(:, :, IZ_SLICE, 1 ); reference=abs(reference);
223
224 tmp1=static1.IMG_anim_mean{end}(:, :, IZ_SLICE, 1); tmp1=abs(tmp1)/sum(abs(tmp1(:)))
225         *sum(reference(:)) ;
226
227 tmp2=static1.IMG_anim_mean_corr{end}(:, :, IZ_SLICE, 1);
228         tmp2=abs(tmp2)/sum(abs(tmp2(:)))*sum(reference(:)) ;
229
230
231
232 subplot(1, 4,1); imshow(tmp1, []); colormap gray; axis off; title('Image w/ motion');
233 subplot(1, 4,2); imshow(tmp2, []); colormap gray; axis off; title('Corrected');
234 m1=min(min(abs(tmp2)-abs(reference)));
235 m2=max(max(abs(tmp2)-abs(reference)));
236 mapping=[m1, m2];
237 rms1=sqrt(sum(sum(abs(tmp1)-abs(reference)).^2)/sum(size(reference(:))-1);
238 rms2=sqrt(sum(sum(abs(tmp2)-abs(reference)).^2)/sum(size(reference(:))-1);
239
240
241 subplot(1, 4,3); imshow(abs(tmp1)-abs(reference), mapping) ; axis off;
242         title('Error (w/motion)'); xlabel(sprintf('RMS=%3.2f', rms1));
243
244 subplot(1, 4,4); imshow(abs(tmp2)-abs(reference), mapping) ; axis off;
245         xlabel(sprintf('RMS=%3.2f', rms2));
246
247
248 axis off; title('Error (corrected)');
249 set(gcf, 'units', 'normalized', 'outerposition', [0 0 1 1]);
250 pngname=sprintf('%s%s', avi_path, 'comp_image_motion_corrected');
251 img=getframe(gcf);
252 imwrite(img.cdata, [pngname, '.png']);
253
254

```

```

255
256
257     %%%%%%%%%%%%%%%%%%%%%%%%%%%%%%%%%%%%%%%%%
258     %%%COMPARISON OF K-SPACES
259     %%%%%%%%%%%%%%%%%%%%%%%%%%%%%%%%%%%%%%%%%
260     figure(); title('K-SPACES for Motion and Motion Corrected vs. STATIC');
261     reference=squeeze(station.sqzrawdata(:,:,IZ_SLICE, 1, 1)); reference=abs(reference);
262     ind1=166:1:285;
263     ind2=1:1:25;
264     tmp2=squeeze(static1.K_chan1_corr(end, :, :, IZ_SLICE));tmp2=
265         abs(tmp2)/sum(sum(abs(tmp2(ind1, ind2))))*sum(sum(abs(reference(ind1, ind2)))) ;
266
267
268     %tmp2=abs(tmp2*sum(reference(:, :))/sum(tmp2(:, 1:50))); %/sum(sum(abs(tmp2)));
269     tmp1=squeeze(static1.K_chan1(end, :, :, IZ_SLICE)); tmp1=abs(tmp1)/
270         sum(sum(abs(tmp1(ind1, ind2)))) * sum(sum(abs(reference(ind1, ind2)))));
271     %tmp1=abs(tmp1 * sum(reference(:, :))/sum(tmp1(:, 1:50))); %/sum(sum(abs(tmp2)));
272
273
274     subplot(1, 5,1); imshow(abs(reference), []); colormap gray; axis off; title('reference');
275
276     subplot(1, 5,2); imshow(abs(tmp1), []); colormap gray; axis off; title('K-SPACE w/ motion');
277     subplot(1, 5,3); I2=imshow(abs(tmp2), []); colormap gray; axis off; title('K-SPACE Corrected');
278
279     m1=min(min(abs(tmp1 )));
280     m2=max(max(abs(tmp1)));
281     mapping=[m1, m2];
282
283
284     subplot(1, 5,4); imshow(abs(tmp1)-abs(reference), [] ); axis off; title('err. (w/motion)');
285     subplot(1, 5,5); imshow(abs(tmp2)-abs(reference), []); axis off; title('err. (corrected)');
286
287     set(gcf, 'units', 'normalized', 'outerposition', [0 0 1 1]);
288     pngname=sprintf('%s%s', avi_path, 'comp_KSPACE_motion_corrected');
289     img=getframe(gcf);
290     imwrite(img.cdata, [pngname, '.png']);
291     %%%%%%%%%%%%%%%%%%%%%%%%%%%%%%%%%%%%%%%%%
292     %%%
293     %%%%%%%%%%%%%%%%%%%%%%%%%%%%%%%%%%%%%%%%%
294     end
295

```

A.0.4 Iterative channel reconstruction/image generation

```

1 function [EIMG_MEAN, K_MEAN, err, IMG_RAW]=create_avg_img_err(sqzrawdata, ky,
2     kz, z_lo, z_hi, IMG_MEAN, err, eflag)
3
4     %error is the input guess vector
5     %eflag is false, then error is calculated (false on first run). if eflag is true,
6     %then input error is used

```

```

7
8 %THIS FUNCTION TAKES IN THE SQUEEZE RAW DATA, AND THE KY AND KZ POINTS
9 %GENERATED BY INFO, AND A GUESS MEANIMAGE (USUALLY CREATED WITH CREATE_avg_IMG)
10 %AND OUTPUTS THE RAW IMAGE FOR THE IC CHANNELS, THE
11 %MEAN IMAGE AVERAGED AS THE GEOMETRIC SUM FOR THE IC CHANNELS, AND THE
12 %MEAN K SPACE AVERAGED OVER THE IC CHANNELS.
13 %IMG_RAW: SIZE IS SAME AS SQZRAWDATA [IX, IY, IZ, IC, IE]
14 %K_MEAN AND IMG_MEAN SIZE IS [IX, IY, IZ, IE]
15 %THE WEIGHTING IS DONE BY THE 1/ERROR^2 AND THE CREATD IMAGE IS
16 %EIMG_MEAN
17
18
19 [IX, IY, IZ, IE, IC]=size(sqzrawdata);
20 %CREATE IMAGE CORRESPONDING TO EACH CHANNEL
21 IMG_RAW=0.0*sqzrawdata;
22 for ie=1:2
23     parfor ic=1:IC
24         IMG_RAW(:, :, :, ie, ic)=fftshift(fftn(sqzrawdata(:, :, :, ie, ic)), 1);
25     end
26 end
27
28
29 if(~eflag)
30     err=zeros(IC, IE);
31     for ie=1:2
32         for ic=1:IC
33             err(ic, ie)=mean(mean(mean(abs(IMG_RAW(:, :, z_lo:z_hi, ie, ic)-
34                 IMG_MEAN(:, :, z_lo:z_hi, ie)).^2)));
35         end
36     end
37     for ie=1:2
38         err(:, ie)=err(:, ie)/sum(err(:, ie));
39     end
40 end
41
42
43 EIMG_MEAN=0.0*IMG_MEAN;
44 % size(EIMG_MEAN)
45 % size(IMG_RAW)
46 for ie=1:2
47     for ic=1:IC
48         EIMG_MEAN(:, :, :, ie)=EIMG_MEAN(:, :, :, ie)+1/IC*1/err(ic, ie)^2*
49             squeeze(IMG_RAW(:, :, :, ie, ic).*conj(IMG_RAW(:, :, :, ie, ic)));
50     end
51 end
52
53 EIMG_MEAN=sqrt(EIMG_MEAN);
54 size(EIMG_MEAN)
55
56 %%INVERSE FOURIER TRANSFORM TO CREATE MEAN KSPACE
57 parfor ie=1:2

```

```

58     K_MEAN(:, :, :, ie)=ifftn(ifftshift(EIMG_MEAN(:, :, :, ie), 1));
59     end
60 end

```

A.0.5 Correct K-Space

```

1 function [K_anim, kxy_p, IMG_anim, IMG_anim_mean, K_anim_mean, K_chan1, times]=
2     corr_animation(input, IZ_SLICE, TSTEP)
3
4     %%THIS FUNCTION TAKES IN THE INPUT STRUCTURE, THE SPECIFIC SLICE, AND THE TIME STEP
5     %%GENERATES THE OUTPUTS REQUIRED FOR THE ANIMATION
6     %times{counter}=[t, iy, iz] time of the animation, the 1:iy points have been filled,
7     and the 1:iz point
8
9     %K_anim{counter}:= animation K-space for the IC channels
10    %kxy_p{counter}:= POINTS IN THE K-SPACE THAT ARE FILLED AT THE CURRENT
11    STEP OF ANIMATION
12
13    %IMG_anim{counter}:= IMAGE GENERATED BY AVERAGING
14    THE 22 CHANNELS USING THE WEIGHTING FACTOR input.err
15
16    %k_anim_mean{counter}:=K space corresponding to IMG_anim{counter}
17
18
19    counter=1;
20
21    K_anim=zeros(input.IX, input.IY, input.IZ, input.IE, input.IC);
22    for iy=1:length(input.ind_hi_y)-1
23        low=input.f_y(iy, 1); %LOWER INDICES TO ITERATE OVER FOR TIME AND Z
24        hi =input.f_y(iy+1, 1); %HIGHER INDICES TO ITERATE OVER FOR TIME AND Z;
25        ky_p=input.f_y(1:iy, 2); %point in y THAT IS BEING ACQUIRED
26        for t=low:hi
27            iz=input.f_z(t); %INDEX OF Z
28
29            %FILL ANIMATION FOR ALL CHANNELS
30            for ic=1:input.IC
31                for ie=1:input.IE
32                    %if(input.ind_corr(t))
33                        K_anim(:,iy,iz,ie,ic)=input.ind_corr(t)*input.sqzrawdata(:,iy,iz,ie,ic);
34                    % sprintf('time t=%d input=%d', t, input.ind_corr(t))
35                    %else
36                    % sprintf('time t=%d K_anim not filled ic=%d', t, ic)
37                    %end
38                end
39            end
40            if (input.ind_corr(t)==1)
41                kxy_p{counter}(:, t)=[iy, iz];
42            else
43                kxy_p{counter}(:, t)=[0 , 0];
44            end

```

```

45
46
47     if(mod(t, TSTEP) == 0 || t==input.f_y(end, 1))
48         K_chan1(counter, :, :, :)=squeeze(K_anim(:, :, :, 1, 1)); %STORE FIRST
49             %CHANNEL ANIMATION K-SPACE
50
51         sprintf('time %d\n', t)
52         %IMG_anim{counter}=0.0*K_anim{counter};
53
54         [IMG_anim_mean{counter}, K_anim_mean{counter}, IMG_anim]=create_avg_img_err(K_anim,
55             input.ky, input.kz, input.z_lo, input.z_hi, input.IMG_MEAN, input.err, 1);
56
57         times{counter}=[t, iy, iz];
58         counter=counter+1;
59         %K_anim{counter}=K_anim{counter-1};
60
61     end
62
63 end
64
65
66 end
67
68

```

A.0.6 Read and sort K-Space trajectory

```

1 function [f_y, ind_hi_y, ind_low_y, dT_y, T_acq_y]=find_index_y(tmp_ky, IC, IE)
2 %%%%%%
3 %%SEARCH THROUGH THE kyvector and find low and high indices
4 %%%%%%
5     count_lo=1;
6     count_hi=1;
7     ind_low_y=0; ind_hi_y=0;
8     low=tmp_ky(1);
9     ind_low_y(1)=1;
10    for j=1:length(tmp_ky)
11        if (tmp_ky(j) ~= low)
12            ind_hi_y(count_hi)=j-1;
13            count_hi=count_hi+1;
14            low=tmp_ky(j);
15            ind_low_y(count_hi)=ind_hi_y(count_hi-1)+1;
16        end
17    end
18    ind_hi_y(end+1)=length(tmp_ky);
19
20
21    %%CALCULATE TOTAL ACQUISITION TIME FOR Y
22    dT_y=ind_hi_y-ind_low_y+1;
23    dT_y=dT_y/IE/IC; %TIME VECTOR FOR Y

```



```

24     T_acq_y=sum(dT_y); %%TOTAL ACQUISITION TIME FOR Y
25     %%CREATE f_y(t)=NSLICE SHEET ACQUIRED AT TIME f_y(j)=(time, ky_point)
26     ti=1;
27     for j=1:length(ind_hi_y)
28         f_y(j, :)=[ti, tmp_ky(ind_hi_y(j))];
29         ti=ti+dT_y(j);
30     end
31 end
32
33 %%%%%%%%%%%%%%%%%%%%%%%%%%%%%%%%%%%%%%%%%%%%%%%%%%%%%%%%%%%%%%%%%%%%%%%%%
34
35 function [f_z, ind_hi_z, ind_low_z, dT_z, T_acq_z, TIME]=find_index_z(tmp_kz, IC, IE)
36     count_lo=1;
37     count_hi=1;
38     ind_low_z=0; ind_hi_z=0;
39     low=tmp_kz(1);
40     ind_low_z(1)=1;
41     for j=1:length(tmp_kz)
42         if (tmp_kz(j) ~= low)
43             ind_hi_z(count_hi)=j-1;
44             count_hi=count_hi+1;
45             low=tmp_kz(j);
46             ind_low_z(count_hi)=ind_hi_z(count_hi-1)+1;
47         end
48     end
49     ind_hi_z(end+1)=length(tmp_kz);
50
51 %%CALCULATE TOTAL ACQUISITION TIME FOR Y
52     dT_z=ind_hi_z-ind_low_z+1;
53     dT_z=dT_z/IE/IC; %%TIME VECTOR FOR Y
54     T_acq_z=sum(dT_z); %%TOTAL ACQUISITION TIME FOR Y
55     ti=1; TIME=[];
56     TIME(1)=ti;
57     f_z=0;
58     for j=1:length(ind_hi_z)
59         f_z(j)=tmp_kz(ind_hi_z(j));
60         ti=ti+dT_z(j);
61         TIME(j)=ti;
62     end
63 end

```

A.0.7 Create Animation

```

1 function [output]=make_movie(input, K_anim, IMG_anim, kxy_p, times, avi_file, IZ_SLICE)
2
3     IX=input.IX;
4     IY=input.IY;
5     IZ=input.IZ;
6     IE=input.IE;
7     IC=input.IC;

```

```

8 DELTA_X=input.DELTA_X;
9 DELTA_Y=input.DELTA_Y;
10
11
12 vidObj=VideoWriter(avi_file);
13 open(vidObj);
14
15 for counter=1:length(kxy_p)
16     if (counter==1)
17         hfig= figure('unit','pixel','position',[DELTA_X*2 100 2*
18             IX+6*DELTA_X 4*IY+6*DELTA_Y],'menubar','none');
19
20         ax1 = axes('parent',hfig,'unit','pixel','position',[2*DELTA_X 4*
21             IY-DELTA_Y 2*IX+DELTA_X IY]);
22
23         xlim([1, IY]); xlabel('KY indices'); ylabel('KZ indices');
24         hold(ax1);title('K SPACE Completion')
25
26         ax2 = axes('parent',hfig,'unit','pixel','position',[2*DELTA_X 3*IY-3*
27             DELTA_Y IX IY], 'XTickLabel',' ',
28
29             'YTickLabel',' '); xlim([0, IX]); ylim([0, IY]); hold(ax2);
30
31         ax3 = axes('parent',hfig,'unit','pixel','position',[4*DELTA_X+IX 3*
32             IY-3*DELTA_Y IX IY], 'XTickLabel','', 'YTickLabel',' '); hold(ax3);
33
34         ax4=axes('parent',hfig,'unit','pixel','position',[2*DELTA_X 2*IY-5*DELTA_Y 2*IX+DELTA_X IY],
35             xlabel('time '); ylabel('motion');hold(ax4);
36
37         mTextBox=uicontrol('style','text');
38         mTextBoxPosition=get(mTextBox, 'Position'); ;
39         mTextBox.Position=[2*DELTA_X 5*IY-0.1*DELTA_Y 2*IX+DELTA_X DELTA_Y];
40         mTextBox.FontSize=20;
41         mTextBox.FontWeight='bold';
42         mTextBox.BackgroundColor='white';
43         set(gcf, 'units', 'normalized', 'outerposition', [0 0 1 1]);
44     end
45     text_box=sprintf('time %5d   IY %3d   IZ %3d \n', input.times{counter}(1),
46         input.times{counter}(2),input.times{counter}(3) );
47
48     set(mTextBox, 'String', text_box);
49
50     plot(ax1, kxy_p{counter}(1, :), kxy_p{counter}(2, :), 'b.');
```

```
59         xlabel('time (s)'); ylabel('motion amplitude (cm)');
60
61     currFrame = getframe(hfig);
62     for dum=1:10
63         writeVideo(vidObj,im2double(currFrame.cdata));
64     end
65     pngname=sprintf('%sing_ZSLICE_%d_t_%d_IY_%d_IZ_%d.png', input.avi_path, IZ_SLICE,
66                     input.times{counter}(1), input.times{counter}(2), input.times{counter}(3));
67
68     print(pngname, '-dpng')
69
70     end
71     close(vidObj);
72     output=1;
73 end
```

REFERENCES

- [1] J. Pauly, “Dixon reconstruction,” 2007.
- [2] A. Deshmane, V. Gulani, M. A. Griswold, and N. Seiberlich, “Parallel mr imaging,” *Journal of Magnetic Resonance Imaging*, vol. 36, no. 1, pp. 55–72, 2012.
- [3] J. F. Glockner, H. H. Hu, D. W. Stanley, L. Angelos, and K. King, “Parallel mr imaging: A user’s guide 1,” *Radiographics*, vol. 25, no. 5, pp. 1279–1297, 2005.
- [4] H. W. Korin, S. J. Riederer, A. E. Bampton, and R. L. Ehman, “Altered phase-encoding order for reduced sensitivity to motion in three-dimensional mr imaging,” *Journal of Magnetic Resonance Imaging*, vol. 2, no. 6, pp. 687–693, 1992.
- [5] N. White, C. Roddey, A. Shankaranarayanan, E. Han, D. Rettmann, J. Santos, J. Kuperman, and A. Dale, “Promo: Real-time prospective motion correction in mri using image-based tracking,” *Magnetic Resonance in Medicine*, vol. 63, no. 1, pp. 91–105, 2010.
- [6] T. S. Sachs, C. H. Meyer, B. S. Hu, J. Kohli, D. G. Nishimura, and A. Macovski, “Real-time motion detection in spiral mri using navigators,” *Magnetic resonance in medicine*, vol. 32, no. 5, pp. 639–645, 1994.
- [7] J. H. Lee, J. M. Pauly, and D. G. Nishimura, “Partial k-space reconstruction for radial k-space trajectories in magnetic resonance imaging,” Oct. 2 2007, uS Patent 7,277,597.
- [8] G. McGibney, M. Smith, S. Nichols, and A. Crawley, “Quantitative evaluation of several partial fourier reconstruction algorithms used in mri,” *Magnetic resonance in medicine*, vol. 30, no. 1, pp. 51–59, 1993.

- [9] A. E. Holland, J. W. Goldfarb, and R. R. Edelman, “Diaphragmatic and cardiac motion during suspended breathing: preliminary experience and implications for breath-hold mr imaging.” *Radiology*, vol. 209, no. 2, pp. 483–489, 1998.
- [10] M. Blaimer, F. Breuer, M. Mueller, R. M. Heidemann, M. A. Griswold, and P. M. Jakob, “Smash, sense, pils, grappa: how to choose the optimal method,” *Topics in Magnetic Resonance Imaging*, vol. 15, no. 4, pp. 223–236, 2004.
- [11] P. M. Robson, A. K. Grant, A. J. Madhuranthakam, R. Lattanzi, D. K. Sodickson, and C. A. McKenzie, “Comprehensive quantification of signal-to-noise ratio and g-factor for image-based and k-space-based parallel imaging reconstructions,” *Magnetic resonance in medicine*, vol. 60, no. 4, pp. 895–907, 2008.
- [12] W. T. Dixon, “Simple proton spectroscopic imaging.” *Radiology*, vol. 153, no. 1, pp. 189–194, 1984.
- [13] J. Nofiele et. al., “Mri compatible motion platform.”
- [14] T. S. Curry, J. E. Dowdey, and R. C. Murry, *Christensen’s physics of diagnostic radiology*. Lippincott Williams & Wilkins, 1990.
- [15] P. Allisy-Roberts and J. R. Williams, *Farr’s physics for medical imaging*. Elsevier Health Sciences, 2007.
- [16] P. C. Lauterbur, “Image formation by induced local interactions: examples employing nuclear magnetic resonance,” 1973.
- [17] J. Ren, I. Dimitrov, A. D. Sherry, and C. R. Malloy, “Composition of adipose tissue and marrow fat in humans by 1h nmr at 7 tesla,” *Journal of lipid research*, vol. 49, no. 9, pp. 2055–2062, 2008.
- [18] L. Brateman, “Chemical shift imaging: a review,” *American Journal of Roentgenology*, vol. 146, no. 5, pp. 971–980, 1986.
- [19] A. Haase, J. Frahm, W. Hanicke, and D. Matthaei, “H nmr chemical shift selective (chess) imaging,” *Phys Med Biol*, vol. 30, no. 4, pp. 341–4, 1985.

- [20] G. Krinsky, N. M. Rofsky, and J. C. Weinreb, “Nonspecificity of short inversion time inversion recovery (stir) as a technique of fat suppression: pitfalls in image interpretation.” *AJR. American journal of roentgenology*, vol. 166, no. 3, pp. 523–526, 1996.
- [21] F. Del Grande, F. Santini, D. A. Herzka, M. R. Aro, C. W. Dean, G. E. Gold, and J. A. Carrino, “Fat-suppression techniques for 3-t mr imaging of the musculoskeletal system,” *Radiographics*, vol. 34, no. 1, pp. 217–233, 2014.
- [22] S. B. Reeder, A. R. Pineda, Z. Wen, A. Shimakawa, H. Yu, J. H. Brittain, G. E. Gold, C. H. Beaulieu, and N. J. Pelc, “Iterative decomposition of water and fat with echo asymmetry and least-squares estimation (ideal): application with fast spin-echo imaging,” *Magnetic resonance in medicine*, vol. 54, no. 3, pp. 636–644, 2005.
- [23] G. H. Glover, “Multipoint dixon technique for water and fat proton and susceptibility imaging,” *Journal of Magnetic Resonance Imaging*, vol. 1, no. 5, pp. 521–530, 1991.
- [24] C. B. Paschal and H. D. Morris, “K-space in the clinic,” *Journal of Magnetic Resonance Imaging*, vol. 19, no. 2, pp. 145–159, 2004.
- [25] R. Mir, A. Guesalaga, J. Spiniak, M. Guarini, and P. Irarrazaval, “Fast three-dimensional k-space trajectory design using missile guidance ideas,” *Magnetic resonance in medicine*, vol. 52, no. 2, pp. 329–336, 2004.
- [26] D. A. Feinberg and K. Oshio, “Ultra-fast multi-section mri using gradient and spin echo (grase) imaging,” Nov. 11 1997, uS Patent RE35,656.
- [27] P. Dimbylow, “FDTD calculations of the whole-body averaged SAR in an anatomically realistic voxel model of the human body from 1 MHz to 1 GHz,” *Physics in medicine and biology*, vol. 42, no. 3, p. 479, 1997.

- [28] H. Yoshioka, N. Takahashi, M. Yamaguchi, D. Lou, Y. Saida, and Y. Itai, “Double arterial phase dynamic mri with sensitivity encoding (sense) for hypervascular hepatocellular carcinomas,” *Journal of Magnetic Resonance Imaging*, vol. 16, no. 3, pp. 259–266, 2002.
- [29] K. P. Pruessmann, M. Weiger, M. B. Scheidegger, P. Boesiger, *et al.*, “Sense: sensitivity encoding for fast mri,” *Magnetic resonance in medicine*, vol. 42, no. 5, pp. 952–962, 1999.
- [30] M. Blaimer, F. A. Breuer, N. Seiberlich, M. F. Mueller, R. M. Heidemann, V. Jellus, G. Wiggins, L. L. Wald, M. A. Griswold, and P. M. Jakob, “Accelerated volumetric mri with a sense/grappa combination,” *Journal of Magnetic Resonance Imaging*, vol. 24, no. 2, pp. 444–450, 2006.
- [31] D. K. Sodickson, C. A. McKenzie, M. A. Ohliger, E. N. Yeh, and M. D. Price, “Recent advances in image reconstruction, coil sensitivity calibration, and coil array design for smash and generalized parallel mri,” *Magnetic resonance materials in physics, biology and medicine*, vol. 13, no. 3, pp. 158–163, 2001.
- [32] M. Uecker, P. Lai, M. J. Murphy, P. Virtue, M. Elad, J. M. Pauly, S. S. Vasanawala, and M. Lustig, “Espirit—an eigenvalue approach to autocalibrating parallel mri: where sense meets grappa,” *Magnetic resonance in medicine*, vol. 71, no. 3, pp. 990–1001, 2014.
- [33] R. Haberman, *Applied partial differential equations: with Fourier series and boundary value problems*. Pearson Prentice Hall Upper Saddle River, 2004, vol. 4.
- [34] M. A. Bernstein, K. F. King, and Z. J. Zhou, *Handbook of MRI pulse sequences*. Amsterdam ; Boston: Academic Press, 2004.

- [35] E. M. Bellon, E. Haacke, P. Coleman, D. Sacco, D. Steiger, and R. Gangarosa, “Mr artifacts: a review,” *American Journal of Roentgenology*, vol. 147, no. 6, pp. 1271–1281, 1986.
- [36] J. P. Hornak, “Basics of nmr,” 1997.
- [37] D. Atkinson, “Motion compensation strategies,” in *Proceeding of the International Society of Magnetic Resonance in Medicine*, 2011, pp. 6–13.
- [38] M. Henningsson and R. M. Botnar, “Advanced respiratory motion compensation for coronary mr angiography,” *Sensors*, vol. 13, no. 6, p. 6882, 2013. [Online]. Available: <http://www.mdpi.com/1424-8220/13/6/6882>
- [39] W. Lin, J. Guo, M. A. Rosen, and H. K. Song, “Respiratory motion-compensated radial dynamic contrast-enhanced (dce)-mri of chest and abdominal lesions,” *Magnetic resonance in medicine*, vol. 60, no. 5, pp. 1135–1146, 2008.
- [40] A. Brau and J. H. Brittain, “Generalized self-navigated motion detection technique: Preliminary investigation in abdominal imaging,” *Magnetic resonance in medicine*, vol. 55, no. 2, pp. 263–270, 2006.
- [41] M. Henningsson and R. M. Botnar, “Advanced respiratory motion compensation for coronary mr angiography,” *Sensors*, vol. 13, no. 6, pp. 6882–6899, 2013.
- [42] S. Thesen, O. Heid, E. Mueller, and L. R. Schad, “Prospective acquisition correction for head motion with image-based tracking for real-time fmri,” *Magnetic Resonance in Medicine*, vol. 44, no. 3, pp. 457–465, 2000.
- [43] J. G. Pipe *et al.*, “Motion correction with propeller mri: application to head motion and free-breathing cardiac imaging,” *Magnetic Resonance in Medicine*, vol. 42, no. 5, pp. 963–969, 1999.
- [44] J. Cai, P. W. Read, J. M. Baisden, J. M. Lerner, S. H. Benedict, and K. Sheng, “Estimation of error in maximal intensity projection-based internal target volume of lung tumors: a simulation and comparison study using dynamic magnetic reso-

- nance imaging,” *International Journal of Radiation Oncology* Biology* Physics*, vol. 69, no. 3, pp. 895–902, 2007.
- [45] C. L. Schultz, R. Alfidi, A. D. Nelson, S. Y. Kopiwoda, and M. E. Clampitt, “The effect of motion on two-dimensional fourier transformation magnetic resonance images.” *Radiology*, vol. 152, no. 1, pp. 117–121, 1984.
- [46] Y. Seppenwoolde, H. Shirato, K. Kitamura, S. Shimizu, M. van Herk, J. V. Lebesque, and K. Miyasaka, “Precise and real-time measurement of 3d tumor motion in lung due to breathing and heartbeat, measured during radiotherapy,” *International Journal of Radiation Oncology* Biology* Physics*, vol. 53, no. 4, pp. 822–834, 2002.
- [47] B. Bussels, L. Goethals, M. Feron, D. Bielen, S. Dymarkowski, P. Suetens, and K. Haustermans, “Respiration-induced movement of the upper abdominal organs: a pitfall for the three-dimensional conformal radiation treatment of pancreatic cancer,” *Radiotherapy and Oncology*, vol. 68, no. 1, pp. 69–74, 2003.
- [48] A. Shankaranarayanan, M. Wendt, J. S. Lewin, and J. L. Duerk, “Two-step navigatorless correction algorithm for radial k-space mri acquisitions,” *Magnetic resonance in medicine*, vol. 45, no. 2, pp. 277–288, 2001.
- [49] T. K. Jhamb, V. Rejathalal, and V. Govindan, “A review on image reconstruction through mri k-space data,” *International Journal of Image, Graphics and Signal Processing (IJIGSP)*, vol. 7, no. 7, p. 42, 2015.